*Response to Revisions*

**Dear Editor van Dinther, Dr. Bauville and Dr. Rosenau,**

**Thank you for these careful revisions. We have made several changes following your constructive comments. The most significant of these changes includes a new supplementary figure (Fig. S5) that shows how frictional work changes when we assume varying ratios of principal stresses (in which the tectonic normal compression exceeds the lithostatic), and how internal work changes when we use different elastic moduli to convert strains to stresses.**

**We respond to individual comments point-by-point below with bolded text. We number our responses for clarity.**

**Sincerely,**
**Jessica McBeck**

*Comments from Referees*

**A. Bauville (Referee)**

abauville@jamstec.go.jp
Received and published: 12 October 2018

General comments:

This article presents a set of laboratory compressive sandbox experiments in association with a detailed analysis and discussion of the mechanical work of the sand pack. During the experiment, the authors monitored forces on the back wall using pressure plates and particle displacement on the side using digital image correlation (DIC). The paper is innovative from the technical point of view. Indeed, using back wall force measurements and DIC, and calling on mechanically motivated assumptions, the authors managed to estimate individual components of the mechanical work in a laboratory experiment. The conclusions confirm the theoretical predictions that were developed in previous publications by the authors. The paper is well organized, the language is good, and the figures are clear. Figures representing graphs are well used (Fig. 3, 4, 8) and are useful to the discussion. Some of the figures showing the experiment and DIC analysis are used more anecdotally (Fig. 2, 5). The literature review is mainly focused on the previous work of the authors and could benefit from being a bit broader, especially regarding older works. In conclusion, this paper is an interesting contribution to the mechanical work of compressive tectonic systems. The focus of the paper is adapted to the journal Solid Earth. I support the publication of this manuscript after some minor corrections.

Arthur Bauville

Specific comments:

As stated above, the literature review is a bit authors-centric. I would like to suggest some readings to broaden a bit the introduction. I listed them at the end of this review.

1) **This is a good point. We now have included additional references throughout the manuscript.**

Fig. 2 and 5 are just used in passing, as a support to Fig. 3 and 4. They could be used a bit better. For example Fig. 2 could be the object of a small paragraph that discusses the dynamics of the experiment and the main events happening before to dive into Fig. 3. In addition, the pre-faulting and post-faulting phases are important events in Fig. 4. The limit pre-post faulting could be indicate on Fig. 2 as well.

2) **We agree that Fig. 2 and Fig. 5 deserve more attention. We now have discussed them in more detail (lines 278-286, lines 349-356).**

Methods A value for the basal friction in the glass and sand detachment experiments should be given here already (it's only given much later in the text).

3) **This important detail is in the Methods section 3.4 (line 223).**

5.59: "We calculated the incremental shear strain fields of each of the views of the sand pack using the curl of the incremental displacement field. " The curl of the incremental displacement field must be the vorticity*char_time, i.e., the rotational part of deformation instead of strain. In 2D the vorticity is a scalar while strain is a tensor. Please explain better what the quantity delta shear strain corresponds to: invariant of the incremental strain tensor? abs(vorticity)? 6.96. Following the previous comments, here, what do you call the shear strain field? the shear strain tensor field of the displacement curl field?

4) **For small angles of rotation, the tangent of that angle is equal to the angle. So, we can calculate the incremental shear strain as the absolute value of the curl of the incremental displacement field. We now include this specification in the methods (lines 166-170).**

Discussion 12.62-65. Here you argue that using lithostatic pressure as the traction on the fault may lead to underestimating Wfric. It would be nice to have an estimate of how much that is. For example, an upper estimate can be given by considering that sigma1 is horizontal and deviatoric stresses are such that yielding occurs. Doing some back of the enveloppe trigonometry on the Mohr-Coulomb diagram I get: Sigma_n = Sigma_mean-(Pl*sin(phi)*tan(phi))/sin(1-phi) where Pl is the lithostatic pressure and phi is the friction angle (you might want to double check my math). Using a friction angle of $30°$ it simplifies to Sigma_n = 2*Pl - (Pl*sin(phi)*tan(phi))/sin(1-phi).

That yields Sigma_n/Pl = 1.35; and at the end of the experiment Wext/(Wgrav+Wfric+Wint)=1.35. That's pretty nice :)

Sigma1 is probably not horizontal which gives you some latitude to put Wprop and Wseism.

5) **We agree that estimating the potential error induced by assuming lithostatic normal compression will benefit this analysis. We have now added a new figure (Fig. S5) showing the impact of using higher estimates of normal compression on the frictional work, and discuss this more thoroughly in the text (lines 395-399).**

Also, the discussion would be a bit more general if you expressed the deficit in percentage in addition to giving the values in mJ.

**6) We have now added this percentage (line 384).**

Technical corrections

2.42: Ritter et al., 2018 -> ref missing

**7) We have added this reference.**

3.72: "In these numerical accretion simulations, all of the work components increase during underthrusting. The development of the new forethrust increases Wint, but decreases Wfric by a greater degree, which correspondingly decreases Wext (Del Castello and Cooke, 2007)." The second sentence seems to contradict the first one.

**8) We have corrected this mistake (lines 73-75).**

4.05 Missing citation for Dotare et al., 2016. Possibly miscited. Do you mean this paper?: Yasuhiro Yamada, Tatsuya Dotare, Juergen Adam, Takane Hori, Hide Sakaguchi. Initiation process of a thrust fault revealed by analog experiments. Geophysical Research Abstracts, 2016, 18

**9) We have added the correct reference (Dotare et al., 2016) to the list.**

4.25. Reverse the order of citations

**10) We have corrected this (line 134).**

9.60. Fig. 3 is cited before Fig. 2. The paragraph can be easily rearranged to avoid that.

**11) We have corrected this with a new paragraph (lines 280-286)**

9.69. Earlier work could be cited (e.g. Vermeer, 1990)

**12) We have added this reference (line 297).**

9.88. Unneeded reference to Fig. 5B 9.93. There is no Fig. 5C 9.94 primary->primarily 10.5. Here you can refer to Fig. 5

**13) We have corrected these mistakes (line 322, lines 349-354).**

Minor comments on figures:

Fig. 3 Panel A has a lot of curves. The curve from exp E374 is hidden behind the others which is a bit unfortunate. Since E373 and E374 are the most important, the drawing order could be changed (i.e. as in the legend). Using thinner lines for E375, E376 could also improe readability Panel B etc-E the light blue curve is hard to distinguish from the grey background

**14) We have modified this figure to improve clarity.**

Suggested readings

Vermeer P. (1990). – The orientation of shear bands. – Géotechnique, 40, 223-234.

Le Pourhiet, Laetitia. "Strain localization due to structural softening during pres- sure sensitive rate independent yielding."Âa˘Bulletin de la Société Géologique de FranceÂa˘184.4-5 (2013): 357-371.

Dahlen, F. A. "Mechanical energy budget of a fold-and-thrust belt."Âa˘NatureÂa˘331.6154 (1988): 335.

Gutscher, MarcâA˘R˘André, et al. "Episodic imbricate thrusting and underthrusting: Analog experiments and mechanical analysis applied to the Alaskan accretionary wedge."Âa˘Journal of Geophysical Research: Solid EarthÂa˘103.B5 (1998): 10161- 10176.

**15) We have now added additional citations to previous work throughout the manuscript.**

**M. Rosenau (Referee)**

rosen@gfz-potsdam.de
Received and published: 15 October 2018

Review of McBeck et al. "The influence of detachment strength. . ."

The paper describes sandbox experiments designed to shed light on the work done in deforming accretionary wedges. It continues a series of papers by the group in considering additional terms of the work budget. A secondary issue is the comparison between two endmember setups of the archetypical sandbox often referred to as "push" vs. "pull". It uses state of the art strain monitoring and force sensing techniques to derive at a more complete work budget formulation.

General comments:

I think this is a landmark paper for modern analysis of a classical experiment and a big step towards a complete work budget of sandbox experiments. The latter is of prime importance when arguing about the dynamic similarity with natural accretionary wedges. Also, giving the increasing resolution of experimental observations requires a re-assessment of the similarity in energetic terms. Only then, new interpretations and implications for nature are possible. I therefore think this paper is a timely and important contribution to be considered for publication after some minor issues are solved as suggested below.

One point that remains unclear to me is the role of Wint (internal deformation). You describe it as elastic strain energy, but is it recoverable? From my experience, I would argue that distributed plastic deformation (compaction) takes up quite a substantial amount (few percent) of the external work applied and should be considered a part of Wint? Could it be useful to add or split off another "damage" term describing the plastic internal work done? Also, the rigidity assumption (1 MPa) seems to me at the lower end (like for a low density, unconfined grain network rather than a well compacted, 5/6-sides confined sand pack) and increasing it could close the gap seen in the work budget. See my comments below on the respective section.

**16) Indeed, $W_{int}$, as calculated, would be recoverable. $W_{int}$ is calculated as the volume integral of the strain energy density (SED) in the region outside the faults in this analysis, and in previous work (e.g., *Cooke and Madden*, 2014). Some portion of the stored strain within the sandpack between the faults may be recoverable upon loading and unloading; such recoverability accounts for the drop in external force upon development of new thrust faults. The off-fault strain measured in the experiments captures the elastic, as well as inelastic and plastic, strain. However, by using elastic constitutive properties to estimate the stresses from the strains, the estimated $W_{int}$ reflects the elastic strain energy density. We have now specified this point in the text (lines 228-230).**

**17) We have now added an additional figure showing how the estimates of $W_{int}$ vary with differing assumed effective elastic moduli (Fig. S5).**

Since the paper has the potential to be an important contribution to the sandbox community, I would suggest adding a paragraph in the discussion where a comparison with natural wedges,

and work done within them, is tried. I think it could be useful to do this to get an idea of how similar experiments are to nature in energetic terms and consequently what new inferences could be drawn from sandbox experiments for the prototype. Given the increasing amount of quantitative observations, the limits of interpretation should be well respected and I think this paper can help a lot in defining those limits.

**18) We have added discussion of these important points, including potential differences between the experiments and crustal prisms, and the limits of potential interpretations (new Section 5.2).**

A minor point is referencing the work of Malte Ritter. In the paper you cite Ritter et al. (2018) but it is not in the reference list, so I cannot judge which of his papers you mean. Since he published two papers in 2018 and one in 2016 (all Ritter et al.), that all fit neatly into this topic, I tried to sort out things below and make suggestions how to include his work here. I think his papers can serve to support your findings nicely.

**19) We have now added the appropriate reference, and included additional references to this work.**

Finally, I suspect you will publish data using GFZ Data Services in the framework of EPOS. Please contact GFZ data services soon enough to allow inclusion of the reference in this paper and register them as "assets" for this article.

**20) We now include the doi to the GFZ data repository for this work.**

Detailed comments:

Page 2 line 42: Ritter et al. (2018): you probably refer to Ritter et al. (2018a, see below). It needs to be added to the Reference list.

**See #19 above.**

Page 4 Line 7 f: The "sandbox rheometry" models by Ritter et al. (2018b) give additional insights into the localization process in wedge experiments. They clearly observe an increase in total work done which is correlated with the onset of diffuse deformation prior to localization. This confirms your hypothesis "Prior to faulting distributed internal strain (Wint) may accommodate a larger percentage of the overall work budget than after thrust fault development,. . ." and may serve as reference here.

**21) This is a good point, and we have added it to the paper (line 112-114).**

Page 5 Line 30 ff: What is the size of the glassbeads used?

**22) We have now added this important detail to the paper (line 135).**

Page 5 line 53 ff: There could be some more, basic information about the imaging setup used (SLR? How much MPx), treatment of distoration, calibration procedure, final resolution of incremental vectorfield/strain field (now in chapter 3.6), imaging frequency with respect to backwall movement (now on page 6 line 75f), software used for DIC. This is very useful

information not only for evaluating the quality of your DIC analysis but will appreciated also by those people setting up new labs and interested in the way to do it.

**23) We have now added these important steps to the Methods section (lines 171-176).**

Page 5 line 57: You refer here to the PHD thesis of Silvan Hoth for DIC. Actually, Adam et al. (2005) is the more proper reference for application of DIC/PIV to sandbox models.

**24) We have replaced this reference with the more appropriate one.**

Page 6 line 74: Why should there be a non-steady state backwall motion. Is this due to the motor, sticky parts of the compliancy of the force sensor-armed backwall? Could this be quantified? I ask because in the end you compare the force readings (at regular temporal intervals) with strain increments (not necessarily at the same regular temporal intervals).

**25) The non-steady backwall motion seems to arise from the screw motor, and not from the sticky parts of backwall-force system. At the slow motor speed used here, we could observe by eye the slowing and speeding up of the motor. So, these differing rates influence the force measurements to the same degree as the strain measurements (observed through DIC). We now include these details in the text (lines 191-194).**

Page 7 line 7ff: It is not entirely clear to me how the distributed strain (diffuse compaction) is related to elastic strain (which should be too small to be observed) given the rigidity of sandpacks? In Figure S2 you use quasi-linear segment of the strain hardening curve – is this really the elastic loading path? The values around 1 MPa appear, as you describe in the Appendix, too low. From every day life experience 1 MPa is what foam has as a Young modulus. What would happen if you consider 100 MPa in your calculation, do the numbers become unrealistic, or may this fill the gap in the work budget described in Ch. 5.1? In general it is not quite clear to me how you calculate Wint (you refer to Cooke and Madden but it would be good to recall it here with a formula and/or figure). When I understand correctly you use the curves such as in fig S2 to derive the stress/strain relationship (elastic modulus) and calculate strain based on the assumption that backwall push is transmitted all over to the opposite side of the experiment (i.e. ratio of backwall displacement and experiment length). If so, I would argue that actual strain is underestimated as experiments with force sensors on both sides (Maillot et al.) showed that force is transmitted only at later stage of such an experiment, when the decollement is closer to the opposite side.

**26) See #16-17 above, and the new supplemental figure (Fig. S5). In addition, we have included further discussion of potential errors in the effective stiffness estimate in the supplementary information. The low apparent stiffness of the sandpack reflects the ease of the sand grains to rearrange rather than the stiffness of the sand particles. For this reason, the relatively low value of stiffness does not surprise us. In the supplemental information, we now discuss how using a shorter compaction length (rather than the full length of the sandpack) impacts the calculation of internal work. Using a length that matches the extent of the high contraction region near the backwall (20 cm) reduces the effective stiffness estimate, and consequently reduces the estimate of internal work. This reduction does not change our general conclusion that internal work comprises a small portion of the energy budget.**

Page 8 line 41ff: The kinematic compatibility assessment is highly appreciated but it may be better placed into the appendix because of the technical character. Probably it is OK if you put the conclusion ("Assessment of the accuracy and precision of the method results in a resolution of incremental vector field of about XX px / YY mm") in chapter 3.2.

**27) We feel that this new approach, although technical in character, deserves to be mentioned in the main text because of its innovation. Many researchers may find this to be a beneficial approach to assess to robustness of their DIC results.**

Page 8 line 55 ff: To better understand the general model evolution I suggest to prepend a short qualitative description of the evolution of the experiments (sequence of faulting, how many thrust in total,. . .) before starting the detailed description. See also comment on Fig3 a below.

**28) We have now added further description of the general evolution of the experiments (line 282-286), including schematics in Fig. 3.**

Page 9 line 70: Ritter et al. (2016) /not (2018) is the actual reference for the weakening behavior of sand and glassbeads faults (also consistent btw with lower absolute stress drops in glassbeads compared to sand).

**29) We have now provided the correct reference.**

Page 10 line 22f and 26f: There seems to be redundancy here!? Page 11 line 31: Fig. 4C not 5C

**30) We have made these corrections.**

Page 12 line 74: Why is Wgrowth not considered here, is it impossible to constrain from the setup?

**31) We cannot robustly estimate the change in shear stress along the sliding faults, so we cannot provide confident estimates. In Section 5.1, we discuss how the contribution of $W_{seis}$ and $W_{grow}$ could contribute to the work budget deficit.**

Figure 3

A: - text: "glass bead detachment"; - it's a bit busy with the combination of 4 setups. Either a different colorcode and bigger, or two plots? - I don't quite understand: Are the peaks labelled fore- and backthrust secondary peaks following the "first thrust pair" peak. In other words: Do those fore-and backthrusts represent the first thrust pair? From the text it appears that these are new thrusts forming after the first pair? To clarify in gneral, I suggest to add a sequence of images showing each stage of new thrust formation covering the full experimental run (the 1000 seconds), probably in appendix? Or a movie of each experiment? And a short qualitative description of the evolution of the experiments in chapter 4.

B-E: - The light vs dark blue is difficult to see. I suggest to use more different colours.

**32) We have now improved the layout and coloring of this figure, including schematic images.**

Figure 4:

- Also quite busy the figures and the different markers and their assignment to experiments and view are not easy to capture.z - Maybe use two transparent bands instead 4 lines to indicate the phase of localization. - Maybe display experiment in individual panels.

**33) We agree that this figure can be confusing at first. However, using two transparent bands increases the complexity because these bands overlap on the plots, producing apparently 3 bars. In addition, we would like to plot the pairs of experiments together in order to better compare the differences and similarities between experiments with glass and sand detachments.**

Page 14 line 34f: I suspect you will publish your data with GFZ Data Services in the framework of EPOS. I so, the sentence should be "Data. . .. Have been uploaded to the GFZ Repository published open access in McBeck et al. (2018)".

**See #20 above.**

References:

Adam, J., J.L. Urai, B. Wieneke, O. Oncken, K. Pfeiffer, N. Kukowski, J. Lohrmann, S. Hoth, W. van der Zee, J. Schmatz, (2005), Shear localisation and strain distribu- tion during tectonic faulting - New insights from granular-flow experiments and high- resolution optical image correlation techniques, Journal of Structural Geology, 27(2), 183-301,doi:10.1016/j.jsg.2004.08.008.

Ritter, M., K. Leever, M. Rosenau, and O. Oncken (2016): Scaling the Sand Box - Mechanical (Dis-) Similarities of Granular Materials and Brittle Rock, J. Geophys. Res - Solid Earth, doi.: 10.1002/2016JB012915.

Ritter, M.C., M. Rosenau, O. Oncken (2018a): Growing Faults in the Lab: Insights into the Scale Dependence of the Fault Zone Evolution Process, Tectonics, doi: 10.1002/2017TC004787

Ritter, M.C., T. Santimano, M. Rosenau, K. Leever, O. Oncken (2018b): Sand- box rheometry: Co-evolution of stress and strain in Riedel– and Critical Wedge– experiments, Tectonophysics, Volume 722, 2 January 2018, Pages 400-409, ISSN 0040-1951, doi: 10.1016/j.tecto.2017.11.018.

—————————end of review———————
Interactive comment on Solid Earth Discuss., https://doi.org/10.5194/se-2018-93, 2018.

# The influence of detachment strength on the evolving deformational energy budget of physical accretionary prisms

Jessica McBeck[1, 2], Michele Cooke[1], Pauline Souloumiac[3], Bertrand Maillot[3], Baptiste Mary[3]

[1] Department of Geosciences, University of Massachusetts Amherst, MA, USA
[2] Now at: Physics of Geological Processes, The Njord Centre, Department of Geosciences, University of Oslo, Norway
[3] Département Géosciences et Environnement, Université de Cergy-Pontoise, Cergy-Pontoise, France

*Correspondence to*: Jessica McBeck (j.a.mcbeck@geo.uio.no)

**Abstract.** Tracking the evolution of the deformational energy budget within accretionary systems provides insight into the driving mechanisms that control fault development. To quantify the impact of these mechanisms on overall system efficiency, we estimate energy budget components as the first thrust fault pair develops in dry sand accretion experiments. We track energy budget components in experiments that include and exclude a basal layer of glass beads in order to investigate the influence of detachment strength on work partitioning. We use the measurements of normal force exerted on the backwall to estimate external work, and measurements of strain observed on the sides of the sandpacks to estimate the internal work, frictional work and work against gravity done within increments of each experiment. Thrust fault development reduces the incremental external work and incremental internal work, and increases the incremental frictional work and incremental gravitational work. The faults that develop within higher friction detachment experiments produce greater frictional work than the faults in experiments with glass bead detachments because the slip distribution along the detachments remain the same while the effective friction coefficient of the detachment differs between the experiments. The imbalance of the cumulative work budget suggests that additional deformational processes that are not fully captured in our measurements of the energy budget, such as acoustic energy, consume work within the deforming wedge.

## 1. Introduction

In accretionary prisms, margin-perpendicular convergence produces distributed layer-parallel compaction ahead of the wedge until strain localizes as slip along discrete frontal thrust faults (e.g., *Koyi*, 1995; *Burberry,* 2015; *Ghisetti et al.*, 2016; *Lathrop and Burberry*, 2017). The frictional strength of the basal detachment and rheology of the wedge control the internal deformation throughout the wedge prior to thrust fault development. Consequently, the timing and geometry of new fault development may vary with varying basal detachment strength.

Understanding the energetic tradeoffs between pervasive internal strain and fault development can help predict the timing and geometry of new frontal accretion thrust faults (e.g., *Del Castello and Cooke,* 2007; *McBeck et al*., 2017). Investigations of the energy available for creating new fault surfaces show that new frontal accretion faults may only develop when the system has stored sufficient energy that can be expended in the development of new faults, which consume both acoustic and propagation energy (*Del Castello and Cooke,* 2007; *Herbert et al.,* 2015). Numerical simulations of physical accretion experiments demonstrate that optimizing the total external work done on the wedge can successfully predict the position and dip of new frontal accretion thrusts (*McBeck et al*., 2017). These and other numerical efforts demonstrate the ability of energy criteria to successfully predict and understand fault development (e.g., *Masek and Duncan,* 1988; *Hardy et al.*, 1998; *Burbidge and Braun,* 2002; *Cubas et al.*, 2008; *Marshall et al.*, 2010; *Dempsey et al.*, 2012; *Mary et al.,* 2013; *Yagupsky et al.,* 2014; *Cooke and Madden,* 2014; *McBeck et al.*, 2016, 2017). However, few studies have used energy criteria to assess fault development within scaled physical analog experiments (e.g., *Ritter et al*., 2018a). In particular, investigations of the energy budget of physical accretion experiments have thus far focused on two components: the external work and work of fault propagation (*Herbert et al*., 2015). The complete deformational energy budget has not been calculated for deforming physical analog accretionary wedges. Calculating the components of the complete energy budget, including the energy consumed in frictional slip, uplift against gravity and internal diffuse deformation, provides a more complete picture of evolving energy partitioning throughout the system, and the tradeoffs between deformational processes associated with each work budget component.

We tracked the complete work budget from the onset of deformation through the formation of the first thrust pair within four scaled dry sand accretion experiments performed at the University of Cergy-Pontoise (UCP). Half of the experiments employed a basal layer of glass beads in order to provide a low friction basal detachment. Digital image correlation (DIC) and force measurements enabled estimation of the energy expended in uplift against gravity, work done against frictional slip, energy stored as pervasive off-fault deformation, and the total external work done on the physical accretion experiments. We compare the evolution of work budget partitioning for experiments with high and low frictional detachments in order to reveal the sensitivity of different processes captured in the work budget on detachment strength.

## 2. Background

Field observations, physical analog experiments and numerical simulations inform the energy budget associated with the spatiotemporal evolution of faults within accretionary systems.

### 2.1. Energy budget of accretionary systems

The material properties that control strain localization and thrust fault development in accretionary prisms include the evolving
frictional strength of the detachment, the internal frictional coefficient and cohesion of the relatively intact material within the
wedge, the evolving cohesion and frictional strength of the thrust faults, and the effective stiffness of the wedge (**e.g., *Davis et al.*,
1984; *Dahlen et al.*, 1984; *Lohrmann et al.*, 2003; *Le Pourhiet*, 2013**). An energy budget framework can quantify the impact of
each of these evolving properties, and the resulting stresses and strains within the wedge, on system deformation (e.g., ***Dahlen*,
1988; *Burbidge & Braun*, 2002**). In particular, recent investigations of fracture propagation and interaction indicate that tracking
the evolution of various components of the work budget of a deforming fault system sheds insight into mechanical processes that
control fault system development (e.g., *Del Castello and Cooke*, 2007; *Dempsey et al.*, 2012; *Cooke and Madden*, 2014; *Herbert
et al.*, 2015; *McBeck et al.*, 2017; ***Newman & Griffith*, 2014**). The energy budget of a deforming fault system includes the internal
work of deformation, $W_{int}$, the work of uplift against gravity, $W_{grav}$, the work done against frictional sliding along fractures, $W_{fric}$,
the work required to create new fracture surfaces, $W_{prop}$, and the work released as seismic energy, $W_{seis}$. The external work, $W_{ext}$,
quantifies overall system efficiency and is the sum of the product of the normal and shear displacements and tractions on system
boundaries.

The evolving energy budget of accretionary systems can help predict the spatiotemporal development of accretion faults (*Del
Castello and Cooke*, 2007; *McBeck et al.*, 2017; ***Burbidge & Braun*, 2002**). *Del Castello and Cooke* (2007) show that accretionary
faults evolve to optimize the total work done in the system, even as individual components of the work budget increase. In these
numerical accretion simulations, the development of the new forethrust increases $W_{int}$, but decreases $W_{fric}$ by a greater degree,
which correspondingly decreases $W_{ext}$ (*Del Castello and Cooke*, 2007). *Del Castello and Cooke* (2007) propose that a fault will
propagate only when the gain in efficiency exceeds the energetic cost ($W_{prop} + W_{seis}$) of propagating the fault. Analysis of the change
in external work associated with the propagation of new faults in physical accretionary wedges indicate that greater energy per
fault area ($W_{prop}$) is expended during fault propagation in thicker sandpacks and higher frictional strength sand (*Herbert et al.*,
2015). *McBeck et al.* (2017) demonstrate that the forethrust geometry that optimizes the overall efficiency of the fault system, $W_{ext}$,
closely matches the position and dip of forethrusts observed in physical accretion experiments. The success of using external work
optimization to assess the geometry and timing of accretion thrust development suggests that an analysis of the entire work budget
throughout the transition from diffuse deformation to localized faulting may provide insight into the processes associated with this
transition.

In this study, we track the evolving energy budget in wedges with detachments of differing strengths in order to assess how
detachment strength influences the overall efficiency of the wedge (external work), as well as the magnitude of fault slip (frictional
work), uplift against gravity (gravitational work) and pervasive internal strain (internal work). We expect that higher detachment
strength may 1) increase external work by providing greater resistance to contraction, 2) increase the frictional work if the
magnitude and distribution of slip along the detachments remain the same and 3) may increase the internal work prior to thrust
faulting due to greater shear tractions on the detachment that produce higher stresses within the wedge.

**2.2. Onset of strain localization in accretionary systems**

Field observations suggest that off-fault deformation within accretionary prisms, such as distributed microcracking and ductile
deformation, produce diffuse thickening of strata that accommodates a significant proportion (30-40%) of total shortening (e.g.,
*Lundberg & Moore*, 1986; *Morgan et al.*, 1994; *Morgan & Karig*, 1995; *Moore et al.*, 2011). Recent retro-deformations of seismic

95 profiles from the central Hikurangi Margin suggest that macroscopic thrust faults and folds accommodate <50% of the margin-perpendicular shortening due to plate convergence (*Ghisetti et al.*, 2016). The protothrust zone identified in seismic transects of the Nankai wedge between the trench and a zone of imbricate thrust faults (e.g., *Moore et al.*, 2011) indicates that diffuse compaction within crustal wedges may be concentrated into particular zones, and not homogeneously distributed throughout the wedge.

100 The million to thousand year intervals between faulting events within crustal accretionary wedges amplifies the need of scaled and quantitatively-monitored physical experiments to directly document the transition from diffuse deformation (i.e. greater internal work) to localized faulting (i.e. greater frictional work). **Recent analytical analyses indicate that the solutions governing the stability and critical taper of non-cohesive accretionary wedges do not differ in subaerial (dry) and submarine (normally pressured) conditions (*Lehner & Schöpfer*, 2018), suggesting that insights from dry physical accretion experiments are**
105 **applicable to submarine, crustal accretionary prisms.** Physical accretion experiments reveal distributed layer-parallel shortening associated with detachment slip prior to the localization of slip along thrust faults (e.g., *Mulugeta & Koyi*, 1992; *Koyi*, 1995; *Burberry,* 2015; *Lathrop & Burberry*, 2017; *McBeck et al.*, 2017). In dry sand accretionary wedges, inclusion of a ductile detachment greatly increases the overall distributed internal strain associated with folding and thrusting (*Lathrop & Burberry*, 2017). Incremental displacement fields of the sides of wedges indicate that short-lived shear bands episodically develop until strain
110 localizes onto a single frontal forethrust (e.g., *Bernard et al.*, 2007; *Dotare et al.*, 2016). The short-lived shear bands contribute to distributed internal deformation prior to localized slip.

**Previous experiments observed transient increases and decreases in external force associated with fault development, indicative of varying magnitudes of external work (*Nieuwland et al.*, 2010; *Cruz et al.*, 2010; *Souloumiac et al.*, 2012; *Herbert et al.*, 2015; *Ritter et al.*, 2018b).** Similarly, the partitioning of the energy budget is expected to differ before and after thrust fault
115 development. Prior to faulting, distributed internal strain ($W_{int}$) may accommodate a larger percentage of the overall work budget than after thrust fault development, when both internal work and localized frictional slip on faults ($W_{fric}$) accommodate the applied deformation. The strength of the detachment is expected to influence energy budget partitioning. In wedges with weaker detachments, frictional work and gravitational work should consume lower portions of the energy budget, whereas internal work may consume a higher portion of the energy budget compared to wedges with stronger detachments.

120 **3. Methods**

To gain insight into the partitioning of energy components during fault development, we use four accretion experiments performed at the University of Cergy-Pontoise (UCP). Here, we describe the setup and quantitative post-processing of the physical experiments. Then, we describe the method of constraining the effective stiffness of the wedges and the calculation of the work budget components using observations from the experiments.

125 **3.1. Design of accretion experiments**

In these experiments, an electric screw motor translated one wall of the experimental apparatus toward the other in order to contract the dry sand wedge. Throughout the duration of each experiment, three cameras captured photos of different views of the sandpack at one second intervals (Fig. 1). One camera took photos of the top of the sandpack while the other two cameras took photos of the

sandpack cross sections through both of the glass sidewalls. In addition, 16 uniaxial strain gauges mounted on the backwall of the
130 experimental apparatus recorded changes in normal force exerted on the backwall throughout the experiment. Previous physical
experiments performed at UCP indicate that variations in normal force on the backwall coincide with fault development (e.g.,
*Souloumiac et al.*, 2012; *Herbert et al.*, 2015).

The sand deposition method strongly controls the density and frictional properties of the system, and thus how the sandpack
accommodates strain (e.g., *Krantz,* 1991; *Lohrmann et al.,* 2003; *Maillot*, 2013). To construct homogeneous and isotropic
135 sandpacks, a sedimentation device, designed and built at UCP, sieves the sand two or three times before deposition (*Maillot*, 2013).
We used this sedimentation device to construct the sandpacks.

To investigate the impact of a weaker basal detachment on the energy budget, two of the experiments included a 0.5 cm thick layer
of glass beads (**median grain size of 160 μm**), while the other two experiments did not include this layer. In the experiments
including the basal glass bead layer, a 4 cm thick layer of CV32 sand overlaid a 0.5 cm thick layer of glass beads. In the experiments
140 excluding the glass bead layer, the initial sandpack had 4 cm thickness. For both experiments, we added a protowedge of sand on
top of the rectangular sandpack to concentrate deformation away from the backwall of the experimental apparatus. The protowedge
slope was the angle of repose of the sand (30°), and the base of the protowedge was 10 cm long.

For each set of two experiments that either include or exclude a glass bead layer, we modified the configuration of the experimental
apparatus in order to remove bias arising from sidewall friction following the methods of *Souloumiac et al.* (2012). Frictional
145 sliding of the sandpack along the glass sidewalls produces a net force vector that has a different direction depending on whether
the base is fixed or moving. The drag of the sidewall produces curvature in the strike of thrusts that is expected to develop concave
to the motor direction. We changed the direction of the sidewall friction drag by switching the position of the backwall with respect
to the motor (Fig. 1). We aim to eliminate the bias in the experimental observations that arises from sidewall friction by synthesizing
observations from the two experiments.

150 In two experiments (E373, E374), the base of the apparatus slid under the fixed backwall (Fig. 1C). In the other experiments (E375,
E376), the base was fixed and the screw motor pushed the backwall so that the sand slid over the stable glass base (Fig. 1D). In
the remaining text, we refer to these different configurations as the *moving base* (E373, E374) and *moving backwall* (E375, E376)
experiments. The opposing apparatus configurations used here were expected to produce only minimal differences in the position
of the thrusts at the sandpack sides because the ratio of the area of the sandpack in contact with the sidewalls to the area in contact
155 with the base was low (~8/100) in these experiments. *Souloumiac et al.* (2012) find that when this ratio is <0.1, the influence of
sidewall friction produces only small changes in the thrust geometry along-strike. The experiments of this study will confirm the
calculations of *Souloumiac et al.* (2012) if the opposing configurations produce minimal changes in the position of the thrust faults
at the sandpack sides. If the work budgets of the experiments with differing configurations also remains similar, then this study
will provide further confirmation that the apparatus configuration has a minimal impact on strain partitioning.

160 **3.2. Incremental displacement and strain fields**

To constrain the active fault geometry and calculate the energy budget components throughout each experiment, we used digital
image correlation (DIC) to calculate the incremental displacement fields of the top and sides of the sandpack (Fig. 2). For each

sequential pair of photos, DIC analysis determines the incremental displacement field at a grid of points via DIC of pixel constellations (e.g., *Adam et al.*, 2005). The incremental displacement fields revealed active thrusts where slip produces sharp gradients in the displacement field (i.e., localized shear and normal strain) (Fig. 2). We calculated the incremental shear strain fields of each of the views of the sandpack using the curl of the incremental displacement field, which **indicates the incremental rotational angle. In our analysis, the tangent of the incremental rotation angle approximately equals the angle (in radians) because we investigate small changes in displacement. Thus, the curl of the incremental displacement field approximately equals the incremental shear strain under these conditions. This calculation of shear strain is independent of coordinate system, so that shear along all orientations have equal representation**.

**To perform DIC, we employed several techniques to produce accurate incremental displacements from the photos. During the experiment, we acquired 10 MB color 24-bit JPEG photographs. We orthorectified the photos to remove distortion near the edges, converted the color photos to gray scale and increased the contrast in order to aid the DIC calculation. We performed these steps, and performed DIC with a triple pass filter, using the PIVlab MATLAB™ plug in (*Thielicke*, 2018). The analysis produced incremental displacements with a spatial resolution of 0.01 cm, and temporal resolution of 2 seconds, or 0.2 mm of applied backwall displacement.**

### 3.3. Force measurements

To capture fluctuations in normal force exerted on the backwall throughout each experiment arising from strain hardening and softening of the sandpack, we used 16 uniaxial strain gauges mounted on plaques in contact with the backwall (blue in Fig. 1C-D). Four plaques each containing four uniaxial strain gauges were connected in series so that the mean strain of the 16 sensors are reported (Fig. S1). Throughout each experiment, uniaxial strain was recorded at 0.1 second intervals. Calibration of the strain gauges to known weights produced a linear relationship of machine strain units to applied weights with $R^2=0.99$ (Fig. S1). We removed noise from the force data with a standard median filter of 30 measurements. This filter of 0.030 mm increments of applied motor displacement removed noise without over-smoothing the peaks and troughs of the force curve.

### 3.4. Estimation of energy budget components

Each of the components of the work budget arise from integrating the product of force and displacement over the corresponding deforming region (e.g., *Cooke and Madden*, 2014). We estimated the incremental gravitational, frictional, internal and external work at stages of the experiments using the incremental displacement fields of the sides of the wedge and the normal force exerted on the physical backwall. Previous work presents the equations for each component of the energy budget (i.e., *Cooke and Madden,* 2014). Here, we describe how we used the experimental measurements to estimate the values used in those equations.

**At the slow stepper motor rate prescribed here (0.1 mm/s), the true motor displacement rate appears to fluctuate within 1 second intervals. We observed this fluctuation in the screw of the screw motor, and in the varying incremental displacements calculated with DIC. Consequently, this fluctuation impacted both the normal force exerted on and displacement of the backwall. We do not observe stepper motor rate fluctuations at time intervals >1 second. Therefore,** to minimize impact of non-steady incremental backwall movement recorded in the 1 second photo intervals, we stacked sequential incremental displacement fields, producing individual incremental displacement fields representing 0.2 mm of applied

displacement over 2 seconds. To track the elapsed time in each experiment, and calculate the external work, we extracted the total backwall displacement from the DIC displacement fields, rather than rely on the prescribed motor rate and elapsed time.

The motor supplies work to the wedge by applying a force to the moving wall as it displaces at the prescribed velocity. The cumulative external work done from the start of deformation to the stage of interest is the area under the force-displacement curve (e.g., *Cooke and Murphy*, 2004). Thus, the external work done in an increment of an experiment may be considered to be the area under the force-displacement curve for that increment of backwall displacement measured from the DIC fields of the top view. To calculate the external work, $W_{ext}$, done in increments of the physical experiment, we used the backwall displacement within each increment measured from the DIC and the force exerted on the backwall. Assuming that the change in force over the increment is linear,

$$\partial W_{ext} = U_n F_n^0 + \frac{1}{2} U_n (F_n^1 - F_n^0) \tag{1}$$

where $U_n$ is the normal displacement within the increment of the experiment, $F_n^0$ is the force at the beginning of the increment, and $F_n^1$ is the force at the end of the increment.

The work against gravity, $W_{grav}$, measures the work of uplift against gravity, and depends on the vertical normal stress and uplift. We used measurements of the density of sandpack produced with the UCP distributor (*Maillot*, 2013) to estimate the vertical normal stress due to lithostatic compression. We integrated the product of this normal compression and the vertical displacement fields of the sandpack sides over the deforming region to estimate $W_{grav}$. We integrated this product over the 1 m width of the sandpack in order to calculate the volumetric $W_{grav}$ throughout the wedge.

The frictional work, $W_{fric}$, done along faults in the experiment is the area integral of the product of slip along faults and the shear traction on the faults along fault surfaces. We estimated the slip along the detachment fault using the horizontal velocity of the sand at the base of the physical experiment calculated through DIC. We constrained the slip along the backthrust and forethrust by integrating the shear strain field near the observed thrusts. We first identified areas of localized slip within the sandpack as locations with incremental shear strain above a critical value (0.0005 in the approximately 0.2 mm displacement increment). We integrated the product of shear strain and shear traction within these regions of high shear strain to calculate $W_{fric}$. To estimate shear traction associated with slip, we used the Coulomb criterion for frictional slip. Assuming no cohesion of the sand grains, the shear traction on the faults is the normal traction multiplied by the sliding friction. We assume lithostatic normal tractions on the thrust and detachment faults. Following laboratory measurements of basal friction of sand and glass beads (*Klinkmüller et al.*, 2016), we used sliding frictions of 0.3 and 0.2 for the detachments that develop within sand and glass beads, respectively. Following laboratory measurements of the effective friction of faults that develop within sandpacks produced by the UCP depositor (*Maillot*, 2013), we used 0.7 for the thrust fault sliding friction. We integrated the product of slip, normal stress and effective friction along the area of the fault surfaces throughout the sand pack in order to calculate $W_{fric}$.

Internal work measures the energy consumed in internal strain of the material as quantified by strain energy density, which is a product of the components of the stress and strain tensors. **Here, we use this quantity to capture the elastic contribution to deformation outside the fault zones. Whereas localized faults within the sandpack deform inelastically, the sandpack around the faults stores and releases strain in concert with fault slip. The overall elastic response of the sandpack produces**

**the observed reduction in external force associated with the growth of new thrusts (Fig. 3A).** To estimate the internal work, $W_{int}$, done via distributed deformation in the sandbox **outside the fault zones**, we implemented Hooke's elasticity laws in order to estimate the incremental stress from the observed incremental strain field. The product of this approximated stress and measured strain field forms the strain energy density, which we integrated through the volume of the sandbox to determine the internal work
235 (e.g., *Cooke and Madden*, 2014). We first integrated the strain field for each of the components of the strain tensor over the area of the deforming region that does not include the fault zones of localized slip (where shear strain exceeds a critical value). Multiplying these values by 1 m gives the strain integrated throughout the volume of the sandpack. Next, we converted the integrated strain tensor components to approximate integrated stress tensor components using Hooke's law for plane strain, which utilize the material properties Poisson's ratio and Young's modulus. We set Poisson's ratio to 0.2, which is within the range of dry
240 sand values from 0.2-0.4 (*Gercek*, 2007). We used our estimates of the effective stiffness of these sandpack for Young's modulus (Sect. 3.5, Fig. S2).

Throughout each experiment, the gravitational, frictional and internal work calculated from the displacement field of one side of the sandpack may differ from the work calculated from the opposite side of the sandpack. These differences arise from changes in the fault geometry along strike, as well as in the quality of the incremental displacements calculated through DIC. Consequently,
245 we present the components calculated from the incremental displacement fields of both sides of each experiment. This demonstrates the variability that can be expected in different accretion experiments (e.g., *Cubas et al.*, 2010).

### 3.5. Constraining effective stiffness with force and strain

The calculation of internal work within the accretion experiment depends on the stress state within the wedge, which is not measured in these experiments. To constrain the internal stress state from the observed strain fields using Hooke's laws and the
250 effective stiffness of the material, we must estimate the effective stiffness of the sand wedges. To do this estimation, we used measurements of the normal force exerted on the backwall and contraction along the sides of the sandpack (Text S1). The slope of the resulting stress-strain curve at 50% of the peak stress reveals the effective stiffness of the sand (e.g., *Barber*, 2002). Like other geotechnical materials with overall non-linear rheology, sand aggregates show linear behavior around 50% of peak stress (e.g., *Klinkmüller et al.*, 2016). Consequently, the slope of the normal stress-normal strain curve preceding thrust fault development
255 provides an acceptable estimate of the stiffness of the wedge to use in the approximations of internal work.

We calculated the tangent of the horizontal longitudinal strain, $\varepsilon_{xx}$, and normal stress on the backwall, $\sigma_n$, over an interval of 1 mm of backwall displacement at 50% peak stress (Fig. S2). Each sandpack was built of the same material, and with the same deposition technique, and so each wedge was expected to have similar effective stiffness regardless of apparatus configurations. Nevertheless, the sandpacks in the moving backwall experiments have slightly higher estimates of effective stiffness (1.2, 1.3 MPa) than the
260 sandpack of the moving base experiments (0.6, 0.9 MPa). Because the evolution of force is similar preceding the peak force in each of the experiments (Fig. 3), differences in the effective stiffness estimates arise from local variations in the sandpack that impact the incremental horizontal displacement fields. **To estimate internal work in Fig. 4 and Fig. 8, we used the mean of the four stiffness measurements (1 MPa). The supplemental information (Fig. S5) considers the influence of using different values of effective stiffness in the calculation of internal work.**

265 ### 3.6. Kinematic compatibility assessment

The accuracy of the incremental displacement field calculated through DIC varied due to slight differences in illumination, focal depth and camera positioning between each experiment, and between each side of one experiment. To assess the robustness of each incremental displacement field, we calculated the 2D kinematic compatibility of each field. We solved the 2D kinematic compatibility equation at all specified points from the strain, $\varepsilon_{ij}$, as

270 $$K = \frac{\partial^2 \epsilon_{11}}{\partial x_2^2} + \frac{\partial^2 \epsilon_{22}}{\partial x_1^2} - 2 \frac{\partial^2 \epsilon_{12}}{\partial x_1 \partial x_2} \qquad (2)$$

Robust incremental displacement fields will have no apparent movement of material in and out of the plane due to artificial noise, so that the kinematic compatibility, $K$, will be zero throughout the field. To derive a representative measure of the artificial noise level throughout each displacement field, we find the mean plus one standard deviation of the $K$ field, $K^F$ (Fig. S3). We considered displacement fields with $K^F$ above one standard deviation from the mean of the $K^F$ of all the fields as unreliable, and we removed

275 these displacement fields from the calculation of the work budget components. Most of the incremental displacement fields of the experiments contained an acceptable amount of artificial noise (Fig. S3D). The incremental displacement fields derived from the photos taken from the camera on the right side of experiment E375 had the highest noise levels, and consequently most of these incremental displacement fields were excluded from the work budget analysis.

## 4. Results

280 First, we describe the relationship between thrust fault development and the overall efficiency of the wedges. Then, we use the experimental data to estimate the changes to the energy budget associated with the development of new accretionary faults. Finally, we link specific deformational processes to the evolution of the work budget components.

### 4.1. Relationship of external work and faulting events

**In the four experiments, the sequence of faulting followed that observed by *Herbert et al.* (2015). The DIC strain fields**
285 **reveal that first, a backthrust-forethrust pair developed near the leading edge of the protowedge (Fig. 2, Fig. 3). Then, a new backthrust propagated in front of the pre-existing backthrust, further from the backwall. Next, a new forethrust propagated in front of the pre-existing forethrust. Finally, a new backthrust-forethrust pair developed in front of the latest forethrust.**

**The evolution of the normal force exerted on the backwall highlights these faulting events (Fig. 3).** The measured backwall
290 force tracks the evolution of external work because the external work is a function of the normal force exerted on the backwall and the applied backwall displacement. For each experiment, the normal force rose to a local maximum (peak) and fell to a local minimum (trough) coincident with new fault development (Fig. 3). Prior to thrust faulting, the backwall force steadily increased as the wedge compacted and thickened, and greater work was required to maintain the backwall velocity. The three different camera views of the physical experiment enabled identification of thrust faulting events at the top of the sandpack and at both sides
295 of the experiment (Fig. 2). The faults, identified as localized shear strain in the side views and normal contraction in the top view, emerged at the top of the sandpack 0.5-1 mm before the force peak as the force curve transitions from linear to the strain-softening behavior (Fig. 3B-E). The force trough occurred after we observed the first evidence of faulting on either side of the experiment, confirming the findings of laboratory rheometric tests that faults within sand continue to weaken with decreasing friction coefficient

as they accrue several millimeters of slip (e.g., **Vermeer, 1990**; *Lohrmann et al.*, 2003; *Ritter et al.*, **2016**). Consistent with findings of *Herbert et al.* (2015), the experiments with glass bead detachments had lower force drops (24-28 N) than the experiments with sand detachments (30-36 N) (Fig. 3A). This result indicates that thrust fault development in wedges with stronger detachments produces greater reduction in $W_{ext}$. Consequently, new fault growth in wedges with stronger detachments is associated with greater increases in mechanical efficiency. Following the force trough, the backwall normal force remained relatively constant in the experiments with weaker detachments, whereas the force began to rise in the experiments with stronger detachments (Fig. 3A). This behavior suggests that wedges with weaker detachments provide less resistance to the continued backwall displacement and so have greater mechanical efficiency than wedges with stronger detachments following faulting.

## 4.2. Energy budget evolution

To determine the contribution of each deformational process to the increase in overall efficiency associated with fault development, we estimated the energy consumed or stored in increments of applied displacement throughout each experiment. First, we calculated each incremental work budget component over successive increments of backwall displacement (Fig. 4). This incremental work corresponds to the rate of work.

Thrust faulting decreased the incremental $W_{ext}$ and incremental $W_{int}$, and increased the incremental $W_{fric}$ and incremental $W_{grav}$ (Fig. 4). The incremental external work, $\delta W_{ext}$, rose from the onset of displacement to ~35 mJ, and then began to fall following thrust fault development (Fig. 4A). Thrust faulting decreased $\delta W_{ext}$ by ~10 mJ, or by 20% of its value preceding faulting. This decrease corresponds to the onset of strain softening as the backwall force curve deviated from its initial linear trend at the onset of loading.

The incremental internal work, $\delta W_{int}$, was elevated preceding thrust fault development, and fell as the thrusts develop (Fig. 4B). Thrust faulting decreased $\delta W_{int}$ by about 0.02 mJ, or by 20-90% of its value preceding faulting. For each experiment, the largest rate of increasing off-fault deformation occurred immediately preceding thrust fault development (Fig. 4B). Experiment E375 most clearly shows this relationship relative to the other experiments. The period of thrust fault growth had a decreasing rate of off-fault deformation accumulation ($\delta W_{int}$) as strain localized onto the faults, rather than accumulating in the surrounding material.

Prior to thrust fault development, work against frictional slip occurred along the basal detachment fault. For each experiment, thrust fault development increased $\delta W_{fric}$ from the values associated with basal detachment slip preceding thrust faulting (Fig. 4C). The growth of the thrust faults produced greater increases in $W_{fric}$ in the sand detachment experiments than the glass detachment experiments. The slip distribution along the detachments are similar, so this difference in $W_{fric}$ arose **primarily** from the greater friction coefficient of the sand detachments (0.3) relative to the glass detachments (0.2) (Fig. S4). After the thrust faults were fully formed (6 mm of backwall displacement), the cumulative slip distribution along the backthrust in experiment E375 (sand detachment) had greater slip than experiment E374 (glass detachment) (Fig. S4), while the forethrust had less slip in the sand detachment experiment. However, the slip distribution along the detachments in both experiments were similar, indicating that the differences in $W_{fric}$ arose from the differing friction coefficients. The difference in the effective friction coefficient of the detachment in the sand (0.3) and glass (0.2) detachment experiment lead to larger detachment contributions to $W_{fric}$ in the sand (256 mJ) compared to the glass (166 mJ) detachment experiment.

Thrust faulting increased $\delta W_{grav}$ (Fig. 4D). The $\delta W_{grav}$ began to increase prior to thrust fault development as the propagation of the detachment from the backwall produced diffuse uplift. The general increase in $\delta W_{grav}$ coincident with thrusting reflected the increased uplift rate associated with slip along the new thrusts. Slip along the thrust faults more efficiently thickened the sandpack

335  than the prefaulting diffuse processes.

Prior to faulting, the increasing external work applied to the wedge was accommodated with increasing internal work, increasing uplift against gravity, and increasing work against frictional sliding along the detachment. The maximum rate of increase in frictional and gravitational work budget components correlates with the minimum incremental external work, minimum rate of increasing internal work and the peak in backwall normal force. After this peak force, the system fails and more work was expended

340  as work against frictional slip and stored as work of uplift against gravity, than stored as internal work. Of the calculated components of the work budget, thrust faulting produced the smallest changes in $\delta W_{int}$, and largest changes in $\delta W_{fric}$.

### 4.3.  Linking the energy budget to deformational processes

The positive values in the incremental energy budgets suggest that the cumulative work components monotonically increase throughout thrust fault development, but at varying rates. The incremental energy budget of the physical experiments indicates that

345  thrust fault development increased $\delta W_{fric}$ and $\delta W_{grav}$, while decreasing $\delta W_{int}$ and $\delta W_{ext}$. With localized slip along the new thrust faults, displacement of the backwall produced smaller increases in the backwall normal force following thrust fault development than preceding development, reducing $\delta W_{ext}$, and so increasing the mechanical efficiency of the system. Prior to thrust faulting, the applied strain was less efficiently accommodated as distributed off-fault deformation, $\delta W_{int}$. Because internal work is a conservative term, the decrease in $\delta W_{int}$ associated with thrust fault development suggests that work stored as internal strain before faulting was

350  expended as other forms of work when fault slip localizes (i.e., $\delta W_{fric}$ and $\delta W_{grav}$).

The vertical displacement fields of the sides of the physical sandpacks demonstrate that diffuse uplift preceded the development of discrete thrusts (Fig. 5). The evolution of $\delta W_{grav}$ (Fig. 4) reflects the broad uplift preceding thrust development, as well as the localized uplift following thrust development. Prior to thrust fault growth, the broad region of uplift developed near the distal tip of the detachment (**Fig**. 5A), increasing $\delta W_{grav}$, and then as slip localized along thrust faults (**Fig**. 5B), $\delta W_{grav}$ remained stable. After

355  thrust fault formation, $\delta W_{grav}$ remained elevated at ~3 mJ relative to the prefaulting stage (Fig. 4D) because slip along the thrust faults continued to promote uplift (**Fig**. 5B). The more effective uplift against gravity associated with slip along the new thrust faults increased $\delta W_{grav}$ when the thrust faults first develop, and then continued slip along the thrust faults produced similar $\delta W_{grav}$ in subsequent stages.

The increase in $\delta W_{fric}$ following thrust fault development (Fig. 6) illuminates the influence of thrust slip partitioning on the accretion

360  experiments energetic evolution. Thrust development increased the total active fault area and fault slip in the system, increasing $\delta W_{fric}$. Thrust faulting in the experiments with the sand detachments produced greater $\delta W_{fric}$ than in the experiments with the glass detachment (Fig. 5C) because the higher friction detachment faults hosted similar slip to the lower friction detachment faults (Fig. S4). The shear strain of the incremental displacement fields of the physical experiment excluding the glass bead layer (E375) show localized slip on the backthrust at the force trough of the experiment (Fig. 6A). However, the experiment including the glass bead

365  layer (E374) produced lower shear strain in the backthrust region at the force trough (Fig. 6B). The entrainment of glass beads at

the root of the forethrust promotes slip on the forethrust at the expense of the backthrust in the glass bead experiments (Fig. 6C, Fig. S4).

Tracking the evolution of the strain tensor components provides insight into internal deformation prior to thrust fault development, which contributes to the internal work of the system (Fig. 7). Preceding faulting in experiment E375, the wedge contracted horizontally and thickened vertically, producing high normal strains dispersed through the wedge, and localized shear strain along the detachment (Fig. 7A-B). With continued backwall displacement, horizontal contraction and vertical extension shifted toward the distal tip of the detachment, where the thrusts ultimately developed, and the zone of high shear strain surrounding the detachment extended further from the backwall. In the incipient stages of thrust development, horizontal contraction and vertical extension concentrated along the incipient thrusts, forming broad bands of high strain a few centimeters thick (Fig. 7C). As the thrust faults slipped, the zones of high horizontal contraction and vertical thickening localized, and shear strain along the forethrust increased while shear strain along the backthrust remained low (Fig. 7D).

## 5. Discussion

Synthesizing quantitative observations from physical experiments reveals energy partitioning associated with thrust fault development. Here, we discuss how the energy budget balanced in these experiments, and the impact of the apparatus design on strain localization.

### 5.1. Balancing the work budget

Evolving diffuse deformation, uplift and localizing strain change the overall work done in the system (Fig. 8). Following the conservation of energy, the total $W_{ext}$ should equal the sum of the work budget components (e.g., *Cooke and Madden*, 2014),

$$W_{ext} = W_{prop} + W_{seis} + W_{int} + W_{grav} + W_{fric} \tag{3}$$

However, in each experiment, the sum of $W_{int}$, $W_{fric}$ and $W_{grav}$ are 100-200 mJ less than $W_{ext}$ after the faults develop, at 6 mm of backwall displacement (Fig. 8), **or 20-40% of $W_{ext}$.** Here, we focus on experiment E376 because its displacement fields have less noise than the other experiments (Fig. S3), but each experiment produces this deficit in the cumulative work budget. Underestimates of $W_{int}$ may arise from errors in estimates of the effective sandpack stiffness. The effective stiffness may be larger at later stages of the experiment after the sand has compacted under horizontal contraction (e.g., *Koyi*, 1995). In addition, the accommodation of localized slip along thrust faults produces more compliant wedges that require less normal force on the backwall with additional deformation (e.g., *McBeck et al.*, 2017). In addition to these temporal variations, the effective stiffness of experimental and crustal wedges will also vary spatially as less dense material in front of the wedge has lower effective stiffness than compacted material within the wedge (e.g., *Wang & Hu*, 2006). Underestimates of $W_{fric}$ may arise from underestimates of the slip along the faults and/or normal tractions acting on the faults. We assume lithostatic compression along the faults. The overall horizontal shortening may produce compressive normal tractions greater than lithostatic along dipping thrust faults. Underestimates of $W_{grav}$ may arise from underestimating the effective density of the sandpack as the wedge evolves and compacts.

To constrain the potential range in error in $W_{int}$ that arises from the chosen effective stiffness, we calculate the incremental $W_{int}$ through experiment E376 using effective stiffnesses ranging from 0.25 to 100 MPa (Fig. S5). Increasing the stiffness by two orders of magnitude from 1 MPa to 100 MPa increases the average $\delta W_{int}$ done throughout the experiment from 0.01 mJ to 0.5–1.3 mJ for the opposite sides of the sandbox. The maximum range of these estimates remain lower than the average $\delta W_{fric}$ (4-10 mJ) and $\delta W_{grav}$ (1.5-3 mJ), confirming that $\delta W_{int}$ consumes less work than the other components of the energy budget.

To constrain the potential range in error in $W_{fric}$ produced by assuming lithostatic normal compression on the thrust faults, we calculate the $\delta W_{fric}$ using differing ratios of the lithostatic stress, $\sigma_2$, and horizontal normal compression that arises from tectonic forces and burial depth, $\sigma_1$ (Fig. S5). Faults with a coefficient of internal friction of 0.6 and low inherent shear strength will form by Coulomb failure at $\sigma_1/\sigma_2$ ratios less than 3 in the deepest portion of these sandpacks (4 cm of 1700 kg/m$^3$ density sandpack, $\sigma_2 = 0.6$ kPa). Increasing the ratio of $\sigma_1/\sigma_2$ from 1 to 3 increases the average $\delta W_{fric}$ throughout experiment E376 from 4 mJ to 6 mJ. Consequently, the true average $\delta W_{fric}$ may be closer to 6 mJ (when $\sigma_1/\sigma_2$=3) than 4 mJ (when $\sigma_1/\sigma_2 = 1$) in experiment E376, reducing the apparent energy budget deficit.

In our calculations of $\delta W_{fric}$, we did not incorporate the contribution of sidewall friction. However, the geometry of the thrust faults suggests that our liberal application of Rain-X to the glasswalls produced surfaces with low friction coefficients. The lack of pronounced curvature of the strike of the thrust faults viewed from the top of the sandpack (Fig. 2, Fig. S5) indicates a minimal impact of sidewall friction, and thus a low sidewall friction coefficient.

Noise in the displacement fields may also have introduced errors into the work budget calculations. However, variations between the true displacement field and calculated displacement field are likely smaller than differences in the displacement fields on different sides of each experiment, where differences in fault geometry influence the displacement fields. Although we do not know the displacements within the center of the sandpack, the record of displacement at the two side windows provides two viable expressions of the experiment's overall deformation. Consequently, we consider the difference in the work budget values calculated for either side as estimates of uncertainty in the calculations. The shaded regions in Fig. 8 show the difference in the values calculated for each side, and function as uncertainty estimates.

The imbalance of the work budget suggests that other processes besides diffuse internal deformation, frictional slip and uplift against gravity consume work. Processes not directly considered in this study include the creation of new fault surfaces, and the generation of seismic energy or acoustic emissions (e.g., *Madden et al.,* 2017; *Herbert et al.,* 2015). Previous investigations of physical experiments indicate that the total work of creating new fault surfaces and released in seismic energy during fault propagation ($W_{prop} + W_{seis} = W_{grow}$) for sandpacks with 3 cm thickness is 385±150 mJ per each m$^2$ of new fault area (e.g., *Herbert et al.,* 2015). Using this relationship and the area of the faults observed in experiment E374, the cumulative $W_{grow}$ after the thrust faults develop is 130±50 mJ, which could account for most but not all of the 200 mJ of work budget deficit (Fig. 8).

### 5.2. Comparison to numerical and crustal accretionary prisms

In these experiments, we find that $W_{fric}$ consumes the largest portion of the energy budget, while $W_{grav}$ and $W_{int}$ consume the smallest portions. After the formation of the first thrust pair, the cumulative $W_{fric}$, $W_{grav}$, and $W_{int}$ consume 65-80%, 15-20%,

**and 2-5% of the cumulative $W_{ext}$, respectively. In a seminal analytical analysis of the mechanical energy budget, *Dahlen* (1988) found a similar partitioning of the energy budget using a critical wedge theory analysis of the fold-and-thrust belt of western Taiwan, with 45% in $W_{fric}$ along the basal detachment, 39% in $W_{grav}$ and 16% in internal dissipation.** However, numerical models of physical accretion experiments that use elastic rheology show a different partitioning of the work budget than documented in these experiments and by ***Dahlen* (1988)**. For example, the elastic models show a larger proportion of internal work to gravitational work (*Del Castello and Cooke*, 2007). In these elastic models, $W_{grav}$ consumes a smaller portion (<10%) of the energy budget than $W_{int}$ (20-30%), and $W_{fric}$ consumes the largest portion (60-70%) throughout an accretion-underthrusting cycle (*Del Castello and Cooke*, 2007). These differences may arise because the sand aggregate deforms as an elastic-perfectly plastic material, whereas individual sand grains deform elastically. Consequently, at the onset of horizontal contraction in the experimental wedges, the sand aggregate compacts, producing stored internal work, but further horizontal contraction induces sand grain rearrangement. This perfectly-plastic sand grain rearrangement produces uplift against gravity ($W_{grav}$) rather than further increases to off-fault deformation ($W_{int}$). Crustal accretionary wedges may deform somewhere between these two end-member rheologies. Sediment aggregates within crustal accretionary wedges are neither ideally linear-elastic nor elastic-perfectly plastic. While these aggregates cannot easily rearrange in response to internal strain, they can develop small folds, faults and microstructures that reduce internal work, and accommodate vertical thickening and horizontal shortening (e.g., *Morgan & Karig,* 1995).

**Recent advanced in field techniques provide insights into the magnitude of $W_{fric}$ during seismic slip. Heat anomalies detected following the Tohoku-Oki earthquake indicate that the earthquake produced 27 MJ/m$^2$ of frictional heat energy per fault area, with 19-51 MJ/m$^2$ in the 91% confidence interval range (*Fulton et al.*, 2013). The low coseismic friction (0.08) estimated by *Fulton et al.* (2013) suggests that the heat produced by frictional sliding may consume a small portion of the total energy budget. Frictional work may be a smaller contribution to the energy budget in crustal environments than in the physical accretion experiments if fluids, melting, thermal pressurization and other processes decrease the effective friction of crustal faults during slip. Future energy budget analyses should endeavor to estimate the proportion of energy consumed in frictional sliding, and other energy budget components, such as the production of fault damage zones, from field observations (e.g., *Shipton et al.*, 2006). The knowledge of the tectonic environments and conditions under which $W_{fric}$ dominates the energy budget may enable estimates of the total system efficiency, $W_{ext}$, from $W_{fric}$ alone. Because numerical analyses demonstrate that $W_{ext}$ can successfully predict fault development (e.g., *McBeck et al.*, 2016, 2017), the ability to estimate total system efficiency from only $W_{fric}$ may enable robust field predictions of fault development.**

### 5.3. Impact of apparatus design on strain partitioning

We expected the opposing apparatus setup to exert only a minimal impact on deformation within the wedge, and the resulting energy budget components, because the ratio of sandpack area in contact with the sidewalls and in contact with the base is <0.1 (*Souloumiac et al.*, 2012). However, this ratio was determined from experiments in which the materials in contact with the base and sidewalls were the same, and so it may not be valid for the experiments with glass beads. If the frictional sliding of the sandpack against the sidewalls has an appreciable influence on thrust fault geometry, then the trace of the thrust faults would curve near the sidewalls. In the top view displacement field, we observe mature thrust fault traces sub-perpendicular to the applied contraction direction across the full width of the sandpack (Fig. 2, Fig. S6). However, when the thrust faults just began to initiate within the center of the sandpack and propagate towards the sidewalls (Fig. 2A), the curvature in the traces of the developing faults was more pronounced than the later mature fault traces (Fig. S6). The resulting difference between the displacement fields viewed through

the sidewalls and the displacements that occur within the center of the sandpack suggest that the energy budget components calculated from the sideview displacement fields may differ from those within the center of the sandpack most significantly before
470 the thrust faults develop across the full sandpack width.

The distribution of internal compaction differs in the sets of experiments with differing apparatus configurations. The moving base compacted a larger volume of the sand pack than the moving backwall prior to thrust fault development (Fig. 9). When only the backwall displaced, the horizontal contraction of the top of the wedge only reveals significant contraction within 10-15 mm of the backwall (Fig. 9B), preceding thrust fault development (0.19 mm backwall displacement). When the base displaced, the strain field
475 reveals compaction at further distances from the fixed backwall (>20 mm) (Fig. 9A). **The experiment setups differ in the area of sidewall where sand grains move relative to the sidewall. A smaller area of the sandpack slides pass the sidewalls in the moving wall experiment than within the moving base experiment. While the influence of sidewall friction on thrust fault curvature is low, non-zero sidewall friction might produce more diffuse compaction prior to fault formation.** These differences in the actively compacting volume influenced the strain done within the compacting volumes visible through the glass
480 sidewalls preceding thrust fault development (Fig. S2). These differences lead to slightly higher estimates of $\delta W_{int}$ in the experiments with moving bases relative to moving backwalls. However, the relative similarity of these $\delta W_{int}$ estimates (<0.01 mJ difference between experiments with moving backwalls and moving bases) suggest that the impact of these differing strain volumes did not significant impact the calculated $\delta W_{in}$.

## 6. Conclusions

485 This study compared the energetic tradeoffs of frictional slip, uplift and distributed off-fault deformation within physical accretion experiments in order to shed insight on the impact of fault development and detachment strength on deformational processes within accretionary environments. We demonstrate that the new experimental set up used here minimizes the effects of sidewall friction on deformation and the subsequent energy budget estimates. This study is the first effort to quantify four components of the deformational energy budget in accretion physical experiments using force and strain measurements. We use these data to calculate
490 external work, internal work of distributed deformation, work against frictional slip and work of uplift against gravity. Constraining the evolving energy budgets of scaled accretion experiments revealed that thrust fault development increased the overall system efficiency, decreasing the incremental external work. Thrust fault development decreased the incremental external work and incremental internal work, and increased the incremental frictional work and incremental work against gravity. The evolution of gravitational work highlighted the broad uplift of the sandpack that begins prior to slip on localized thrust faults. Variations in the
495 frictional work reveal that lower friction coefficients, as well as lower slip on the backthrust and detachment in the wedges with lower strength detachments suppressed the increase in frictional work arising from thrust fault development in these experiments relative to the higher strength detachment experiments. The imbalance of the cumulative energy budget indicates that additional processes besides those captured here, such as the work of propagation and acoustic energy, may consume a significant portion of the energy budget.

500 **Acknowledgements**

**References**

505 Adam, J., Urai, J., Wieneke, B., Oncken, O., Pfeiffer, K., Kukowski, Lohrmann, J., Hoth, S., van der Zee, W., Schmatz, J.,: Shear localisation and strain distribution during tectonic faulting - New insights from granular-flow experiments and high- resolution optical image correlation techniques, Journal of Structural Geology, 27(2), 183-301,doi:10.1016/j.jsg.2004.08.008, 2005.

Barber, J.: Elasticity: Second Edition. Solid Mechanics and its Applications, 107. Kluwer Academic Publishers, 2002.

Bernard, S., Avouac, J.-P., Dominguez, S., and Simoes, M.: Kinematics of fault-related folding derived from a sandbox experiment,
510 J. Geophys. Res., 112, B03S12, doi: 10.1029/2005JB004149, 2007.

Burbidge, D.R., and Braun, J.: Numerical models of the evolution of accretionary wedges and fold-and-thrust belts using the distinct-element method, Geophys. J. Int., 148, 542-561, 2002.

Burberry, C. M.: Spatial and temporal variation in penetrative strain during compression: Insights from analog models. Lithosphere, 7(6), 611-624, 2015.

515 Cooke, M.L., and Madden, E. H.: Is the Earth lazy? A review of work minimization in fault evolution, J. Struct. Geol., 66, 334–346, doi:10.1016/j.jsg. 2014.05.004, 2014.

Cooke, M.L., and Murphy, S., Assessing the work budget and efficiency of fault systems using mechanical models. J. Geophys. Res: Solid Earth, 109(B10): 2004.

Cruz, L., Malinski, J., Wilson, A., Take, W., and Hilley, G., Erosional control of the kinematics and geometry of fold-and-thrust
520 belts imaged in a physical and numerical sandbox, J. Geophys. Res., 115, B09404, doi:10.1029/2010JB007472, 2010.

Cubas, N., Leroy, Y., and Maillot, B.: Prediction of thrusting sequences in accretionary wedges, J. Geophys. Res., 113, B12412, doi:10.1029/2008JB005717, 2008.

Cubas, N., Maillot, B., & Barnes, C.: Statistical analysis of an experimental compressional sand wedge. Journal of Structural Geology, 32(6), 818-831, 2010.

525 Dahlen, F.A.: Mechanical energy budget of a fold-and-thrust belt. Nature, *331*(6154), 335, 1988.

Dahlen, F. A., Suppe, J., and Davis, D.: Mechanics of fold-and-thrust belts and accretionary wedges: Cohesive Coulomb theory. J. Geophys. Res.: Solid Earth, 89(B12), 10087-10101, 1984.

Davis, D., Suppe, J., and Dahlen, F.A.: Mechanics of fold-and-thrust belts and accretionary wedges. J. Geophys. Res.: Solid Earth, 88(B2), 1153-1172, 1983.

530 Del Castello, M., and Cooke, M.L.: Underthrusting-accretion cycle: work budget as revealed by the boundary element method, J. Geophys. Res., 113, B12404, 1–14, doi:10.1029/2007JB004997, 2007.

Dempsey, D., Ellis, S., Archer, R., and Rowland, J.: Energetics of normal faults earthquakes on dip slip faults. Geology, 79-282. http://dx.doi.org/10.1130/ G32643.1, 2012.

Dotare, T., Yamada, Y., Adam, J., Hori, T., & Sakaguchi, H.: Initiation of a thrust fault revealed by analog 535 experiments. *Tectonophysics*, *684*, 148-156, 2016.

Fulton, P. M., Brodsky, E., Kano, Y., Mori, J., Chester, F., Ishikawa, T., Harris, R., Lin, W., Nobuhisa Eguchi, and Toczko, S.: Low coseismic friction on the Tohoku-Oki fault determined from temperature measurements. *Science* 342, 1214-1217, 2013.

Gercek, H.: Poisson's ratio values for rocks. International Journal of Rock Mechanics and Mining Sciences, 44(1), 1-13, 2007.

Ghisetti, F., Barnes, P., Ellis, S., Plaza-Faverola, A., and Barker, D.: The last 2 Myr of accretionary wedge construction in the 540 central Hikurangi margin (North Island, New Zealand): Insights from structural modeling, Geochem. Geophys. Geosyst., 17, 2661–2686, doi:10.1002/2016GC006341, 2016.

Hardy, S., Duncan, C., Masek, J., & Brown, D.: Minimum work, fault activity and the growth of critical wedges in fold and thrust belts, Basin Res., 10, 365–373., doi:/10.1046/j.1365-2117.1998.00073.x, 1998.

Herbert, J.W., Cooke, M., Souloumiac, P., Madden, E., Mary, B.C., & Maillot, B.: The work of fault growth in laboratory sandbox 545 experiments, Earth Planet. Sci. Lett., 432, 95-102, 2015.

Klinkmüller, M., Schreurs, G., Rosenau, M., & Kemnitz, H.: Properties of granular analogue model materials: A community wide survey. Tectonophysics, 684, 23-38, 2016.

Koyi, H.: Mode of internal deformation in sand wedges. Journal of Structural Geology, 17(2), 293297-295300, 1995.

Krantz, R.W.: Measurements of friction coefficients and cohesion for faulting and fault reactivation in laboratory models using 550 sand and sand mixtures, Tectonophysics, 188 (1–2), 203–207, doi:10.1016/0040-1951[91]90323-K, 1991.

Lathrop, B.A., & Burberry, C.M.: Accommodation of penetrative strain during deformation above a ductile décollement. Lithosphere, 9(1), 46-57, 2017.

Le Pourhiet, L.: Strain localization due to structural softening during pressure sensitive rate independent yielding. Bulletin de la Société Géologique de France, 184(4-5), 357-371, 2013.

555 Lehner, F. K., & Schöpfer, M. P.: Slope stability and exact solutions for cohesive critical Coulomb wedges from Mohr diagrams. Journal of Structural Geology, doi: 10.1016/j.jsg.2018.04.021, 2018.

Lohrmann, J., Kukowski, N., Adam, J., & Oncken, O.: The impact of analogue material properties on the geometry, kinematics, and dynamics of convergent sand wedges, J. Struct. Geol., 25, 1691–1711, doi:/10.1016/S0191- 8141[03]00005-1, 2003.

Lundberg, N. & Moore, J.: Macroscopic structural features in Deep Sea Drilling Project cores from forearc regions. Geological
560 Society of America Memoirs, 166, 13-44, 1986.

Maillot, B.: A sedimentation device to produce uniform sand packs, Tectonophysics, 593, 85–94, doi:/10.1016/j.tecto.2013.02.028, 2013.

Marshall, S.T., Kattenhorn, S., & Cooke, M.: Secondary normal faulting in the Lake Mead fault system and implications for regional fault mechanics. Geological Society of America Special Papers, 463, 289-310, 2010.

565 Mary, B.C.L., Maillot, B., & Leroy, Y.: Deterministic Chaos in frictional wedges revealed by convergence analysis, Int. J. Num. Anal. Methods Geomech., 37, 3036–3051, http://dx.doi.org/10.1002/nag.2177, 2013.

Masek, J.G. & Duncan, C.: Minimum-work mountain building. Journal of Geophysical Research: Solid Earth, 103(B1), 907-917, 1998.

McBeck, J., Madden, E., & Cooke, M.: Growth by Optimization of Work (GROW): A new modeling tool that predicts fault growth
570 through work minimization. Computers and Geosciences, 88, 142-151, 2016.

McBeck, J. A., Cooke, M. L., Herbert, J. W., Maillot, B., & Souloumiac, P.:  Work optimization predicts accretionary faulting: An integration of physical and numerical experiments. Journal of Geophysical Research: Solid Earth, 122(9), 7485-7505, 2017.

McBeck, J., Cooke, M., Souloumiac, P., Maillot, B., Mary, B.: Supplement to: "The influence of detachment strength on the
575 evolving deformational energy budget of physical accretionary prisms". GFZ Data Services. http://doi.org/10.5880/fidgeo.2018.021, 2018.

Morgan, J.K., & Karig, D.: Kinematics and a balanced and restored cross-section across the toe of the eastern Nankai accretionary prism. Journal of Structural Geology 17, 31–45, 1995.

Morgan, J.K., Karig, D., & Maniatty, A.: The estimation of diffuse strains in the toe of the western Nankai accretionary prism: A
580 kinematic solution. Journal of Geophysical Research: Solid Earth, 99(B4), 7019-7032, 1994.

Morgan, G. F., Saffer, D., Studer, M., & Costa Pisani, P.: Structural restoration of thrusts at the toe of the Nankai Trough accretionary prism off Shikoku Island, Japan: Implications for dewatering processes. Geochemistry, Geophysics, Geosystems, 12(5), 2011.

Mulugeta, G., & Koyi, H.: Episodic accretion and strain partitioning in a model sand wedge, Tectonophysics, 202(2), 319-333, 1992.

585 Nieuwland, D. A., Urai, J. L., & Knoop, M.: In-situ stress measurements in model experiments of tectonic faulting. In *Aspects of Tectonic Faulting* (pp. 155-166). Springer, Berlin, Heidelberg, 2010.

Newman, P. J., & Griffith, W. A.: The work budget of rough faults. Tectonophysics, 636, 100-110, 2014.

Ritter, M., Leever, K., Rosenau, M., & Oncken, O.: Scaling the Sand Box - Mechanical (Dis-) Similarities of Granular Materials and Brittle Rock, J. Geophys. Res.: Solid Earth, 121, 6863-6879, doi.: 10.1002/2016JB012915, 2016.

590 Ritter, M.C., Rosenau, M., and Oncken, O.: Growing Faults in the Lab: Insights into the Scale Dependence of the Fault Zone Evolution Process, Tectonics, 37, 140-153, doi:10.1002/2017TC004787, 2018a.

Ritter, M.C., Santimano, T., Rosenau, M., Leever, K., & Oncken, O.: Sand- box rheometry: Co-evolution of stress and strain in Riedel– and Critical Wedge–experiments, Tectonophysics, 722, 400-409, doi: 10.1016/j.tecto.2017.11.018, 2018b.

Shipton, Z.K, Evans, J.P., Abercrombie, R.E. & Brodsky, E.E.: The missing sinks: slip localization in faults, damage zones, and 595 the seismic energy budget. In Abercrombie, R. (Eds) Earthquakes: Radiated Energy and the Physics of Faulting, pages pp. 217-222. Washington, DC.: AGU, 2006.

Souloumiac, P., Maillot, B., & Leroy, Y.: Bias due to side wall friction in sand box experiments, J. Struct. Geol., 35, 90-101, doi:10.1016/j.jsg.2011.11.002, 2012.

Thielicke, W.: PIVlab - particle image velocimetry (PIV) tool. (https://www.mathworks.com/matlabcentral/fileexchange/27659-600 pivlab-particle-image-velocimetry-piv-tool), MATLAB Central File Exchange, 2018.

Vermeer, P. A.: The orientation of shear bands in biaxial tests. Geotechnique, 40(2), 223-236, 1990.

Wang, K., & Hu, Y.: Accretionary prisms in subduction earthquake cycles: The theory of dynamic Coulomb wedge. Journal of Geophysical Research: Solid Earth, 111(B6), 2006.

Yagupsky, D.L., Brooks, B., Whipple, K., Duncan, C., & Bevis, M.: Distribution of active faulting along orogenic wedges: 605 minimum-work models and natural analogue, J. Struct. Geol., 66, 90–101, doi:10.1016/j.jsg.2014.05.025, 2014.
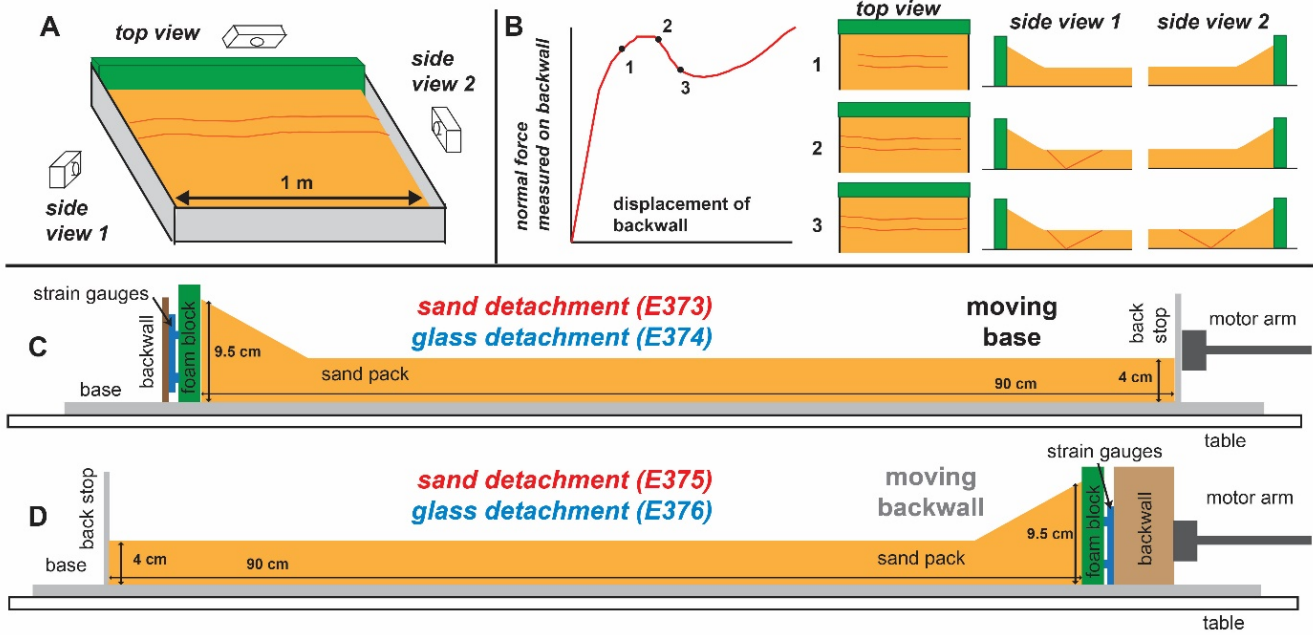
**Figure 1: Schematics of experimental setup, force and faulting evolution. A) Position of cameras relative to sandpack. Backwall and glass**
610 **sidewalls are in green and gray. B) Characteristic force curve and faulting events revealed through the top and side views. C-D)**
**Experiment apparatus configurations of each experiment. The four experiments differ in the apparatus configuration: C) moving base**
**(E373, E374) or (D) moving backwall (E375, E376), and the inclusion of basal glass bead layer.**

20
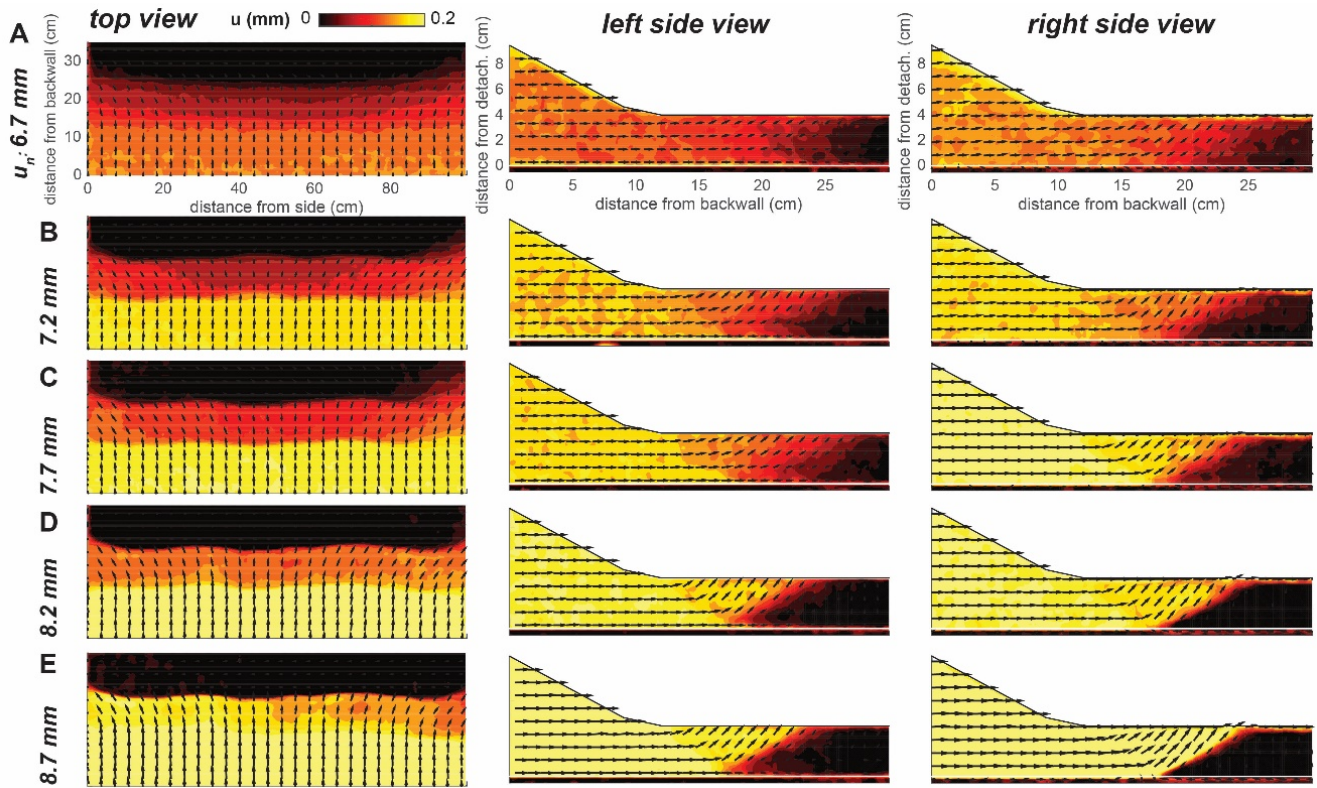
**Figure 2: Incremental displacement fields of top and side views of experiment E374 (glass detachment and moving base) throughout the development of the first thrust pair at 0.5 mm increments of applied backwall displacement, $u_n$. A) Preceding thrust fault development, the net displacement gradually decreases from the backwall toward the opposite wall. B) When sharp gradients in the top view displacement field revealed the development of the first thrust pair within the center of the box, the side view displacement fields showed more diffuse zones of shear. C-E) With continued backwall displacement, the gradients in the top and side view displacement fields progressively sharpened as faults localize. The top view displacement fields reveal that the thrusts began to localize within the center of the sandpack, and then extended toward the sidewalls. The side view displacement fields indicate that fault localization began earlier on the right side than the left side in this experiment (C). The forethrust remained more diffuse on the left side view than the right side view in the last increment shown here (E).**

**Figure 3: Backwall normal force curves with faulting events. A) Force curves throughout complete experiments. The development of thrust pairs produced larger force drops than the development of the singular thrusts. The singular thrusts produced smaller force drops in the experiments with glass detachments than in the experiments with the sand detachments. B-E) Force drops associated with the first episode of faulting in each experiment. Vertical lines indicate when we first observed evidence of localized faulting on the top (black), left side (yellow), and right side (light blue) of the sandpack. Triangles indicate local maximum (peak, upward triangle) and local minimum (trough, side triangle) of first force drop.**
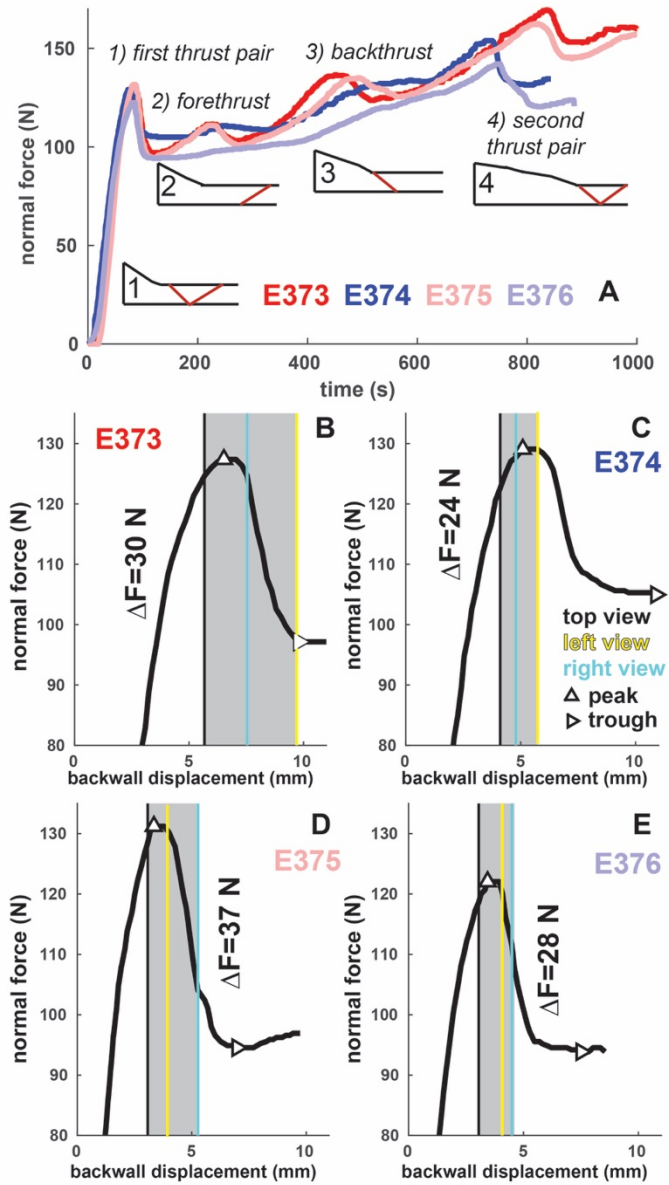
**Figure 4: Incremental work budget components throughout the development of first thrust pair for experiments with the sand detachment (left column), and glass detachment (right column). A) Incremental external work, δW_ext. B) Incremental internal work, δW_int. C) Incremental frictional work, δW_fric. D) Incremental gravitational work, δW_grav. Vertical dashed and solid lines show stages before and after fault development, respectively. We used the displacement fields observed on the left (upward facing triangles and squares) and right (right facing triangles and circles) sides of the box to calculate δW_int, δW_fric and δW_grav. Shaded regions are bounded by curves that are 5-point (for δW_ext) or 20-point (for the other components) median filters through the data obtained from each work budget component. We use a smaller filter window for δW_ext in order to capture fluctuations produced by variations in backwall force, which are lost with a 20-point median filter.**



23
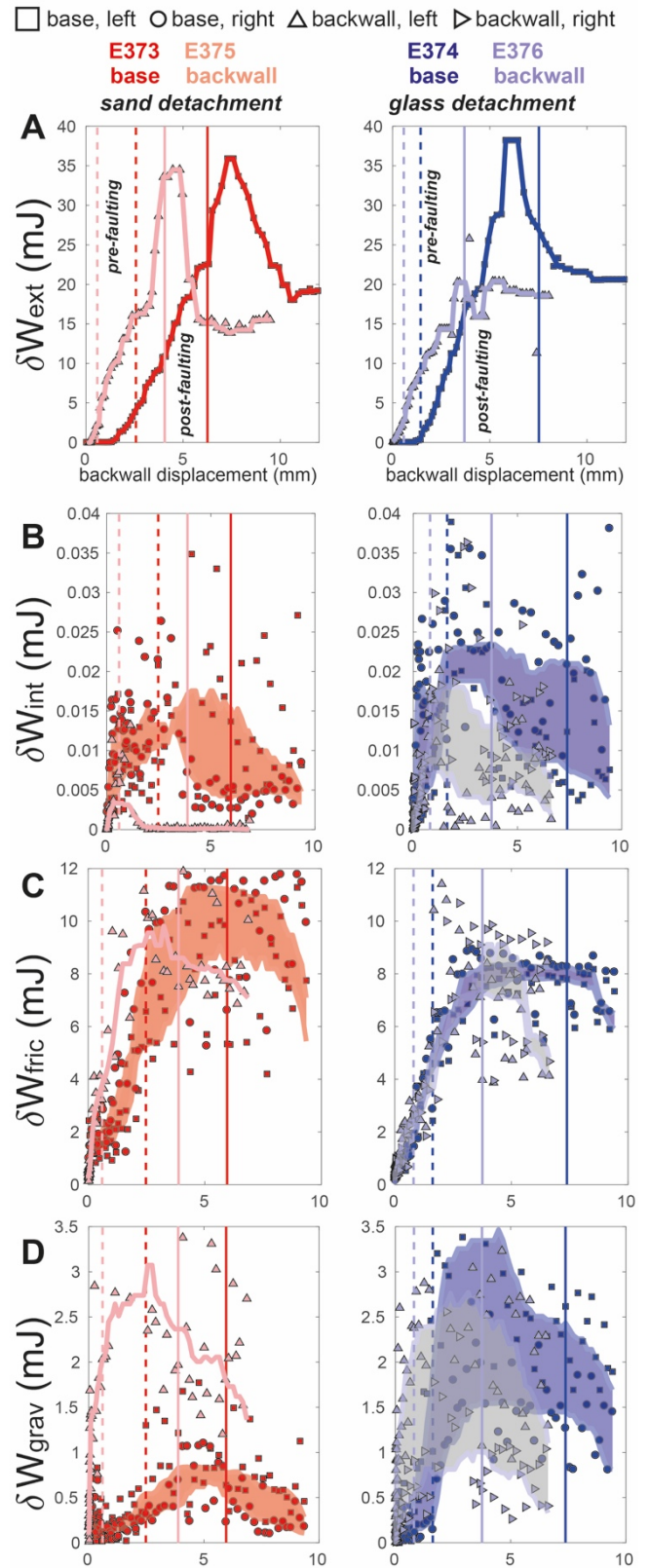
**Figure 5: Vertical displacement fields of moving backwall experiment excluding glass bead layer (E375) preceding (A) and following (B) thrust fault development. Preceding thrust development, a broad pattern of uplift forms in the region where the faults ultimately localize. Following thrust development, uplift localizes above discrete thrust faults. As the uplift pattern transitions from gradational to sharply bounded by faults, the overall $\delta W_{grav}$ increased (Fig. 4).**
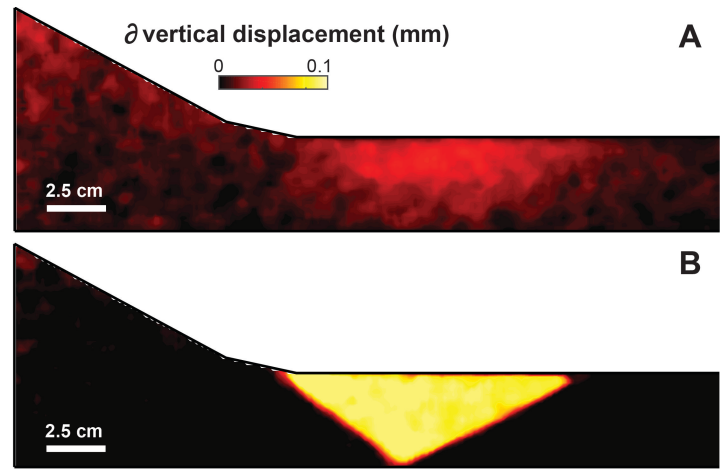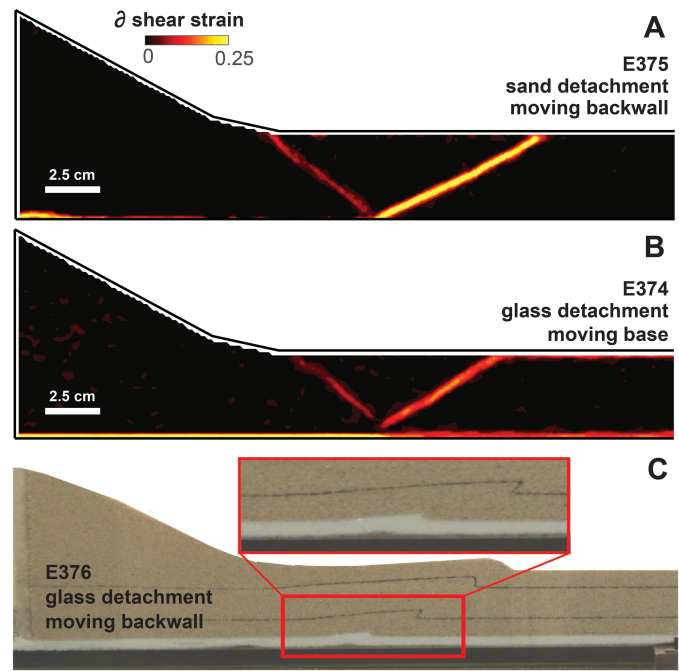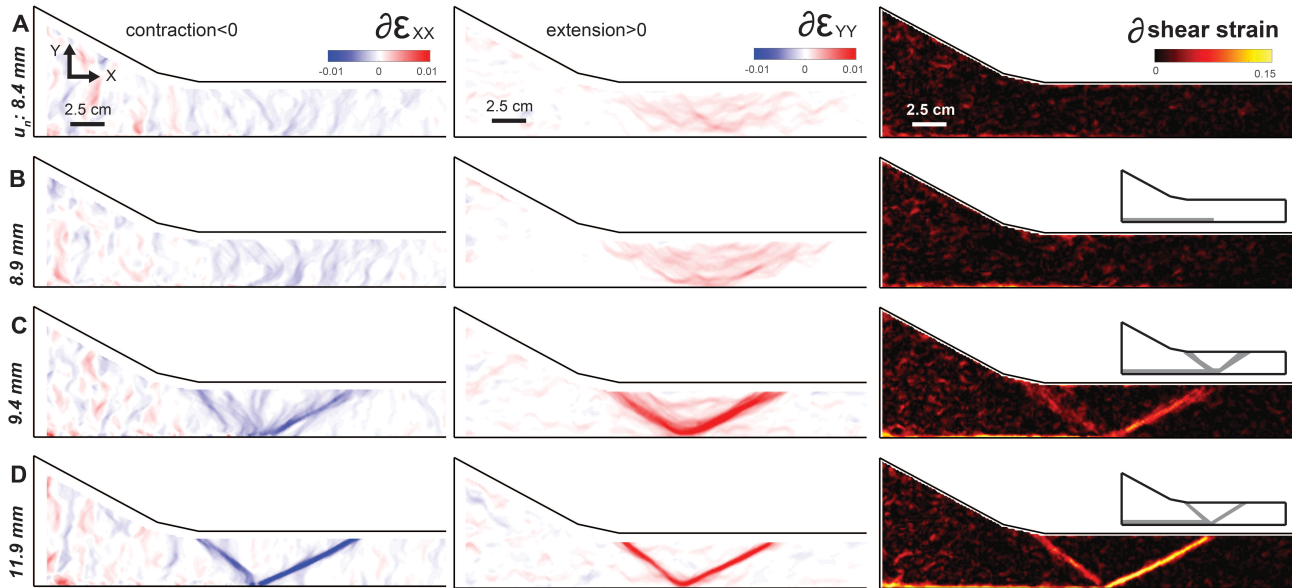
660

665

24

**Figure 6: Shear strain of incremental displacement fields of experiments excluding (A) and including (B) glass bead layer following faulting. The shear strain fields reveal that the inclusion of a glass bead layer suppresses slip on the thrusts. C)**
670 **Photo of side of experiment E376 following faulting. The entrainment of glass beads along the forethrust promoted slip on the forethrust and suppressed the localization of the backthrust, perhaps by producing a smoother transition zone near the base of the forethrust. This suppression of slip on the thrusts reduced**
675 **the change in δ$W_{fric}$ produced by thrust faulting in experiment E374 (glass detachment) relative to that change in experiment E375 (sand detachment).**



∂ shear strain

0    0.25

A

E375
sand detachment
moving backwall

2.5 cm

B

E374
glass detachment
moving base

2.5 cm

C

E376
glass detachment
moving backwall

25

**Figure 7: Evolution of strain as the thrust faults develop in experiment E375. Gray regions in sketches in right column indicate portion of strain field that contributes to $\delta W_{fric}$, and the remaining white area contributes to $\delta W_{int}$. A) Preceding thrust faulting, the wedge had distributed high horizontal and vertical normal strains. B) With continued backwall displacement, horizontal contraction and vertical extension shifted toward the region where the thrusts ultimately develop. C) In the incipient stages of thrust development, horizontal contraction and vertical extension formed broad bands of high strain a few centimeters thick, and shear strain began to localize along both thrusts. At this stage, and in subsequent increments, the forethrust produced higher shear strain than the backthrust. D) The zones of high horizontal contraction, vertical extension and shear strain localized into discrete zones of higher incremental strains along the thrusts. The progressively localizing normal and shear strains produced the gradually increasing and decreasing $\delta W_{int}$ coincident with fault development. Preceding fault development, the distributed strains produced maxima values of $\delta W_{int}$. As strain localizes onto faults, $\delta W_{int}$ decreased to near zero, while $\delta W_{fric}$ increased.**
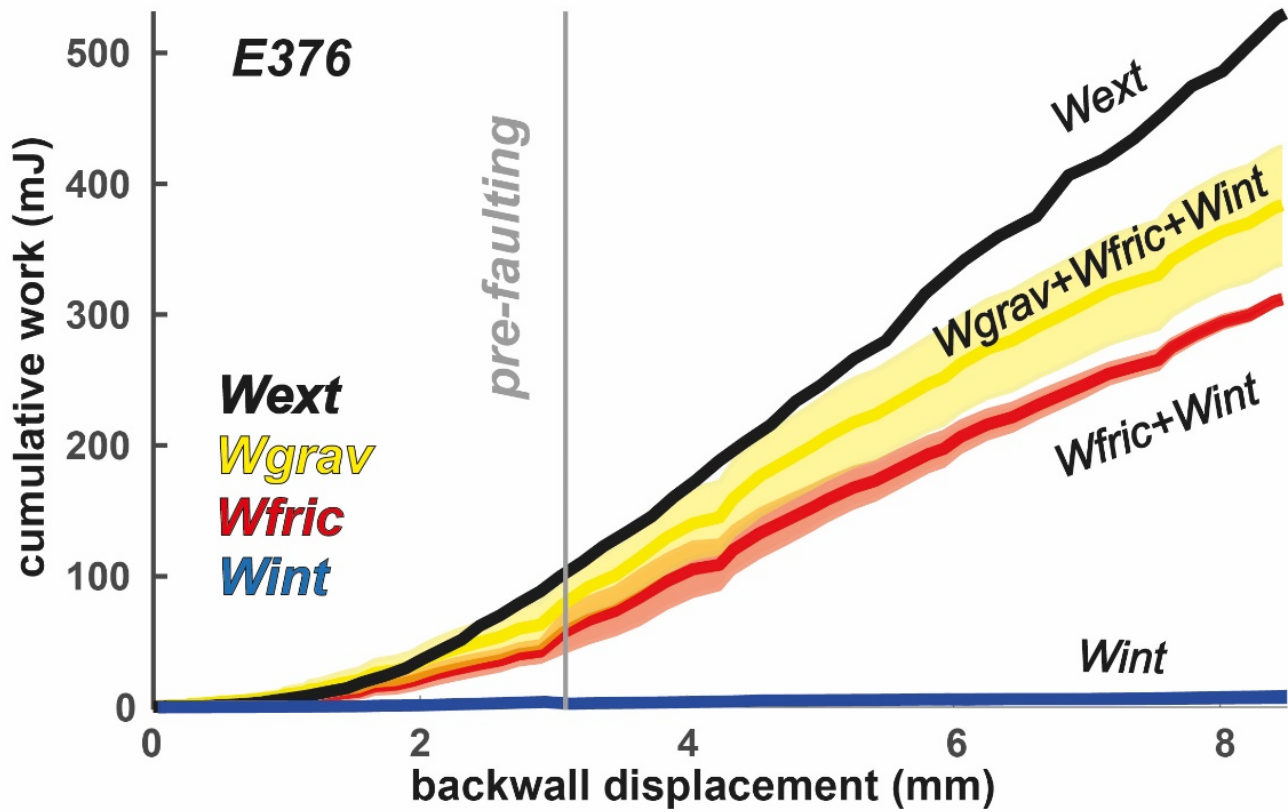
690

**Figure 8: Total accumulation of work done throughout experiment E376. Upper black line shows total W_ext. Thicker lines show accumulation of work components calculated from average of the left and right displacement fields. Upper and lower edges of shaded regions show work accumulation calculated from left and right side views, respectively.**

695

700

**Figure 9: Normal strain perpendicular to the backwall from top views of experiment A) E374 (moving base) and B) E376 (moving backwall). Contraction is negative. Y-axis is perpendicular to the backwall. Red numbers show the cumulative backwall displacement. The motor is located at the top in the moving base (A) and at the bottom in the moving backwall (B) experiment. Preceding thrust fault development, the extent of the compacting region differed depending on the apparatus configuration. This difference produces changes in the effective stiffness estimates, and internal work estimates.**
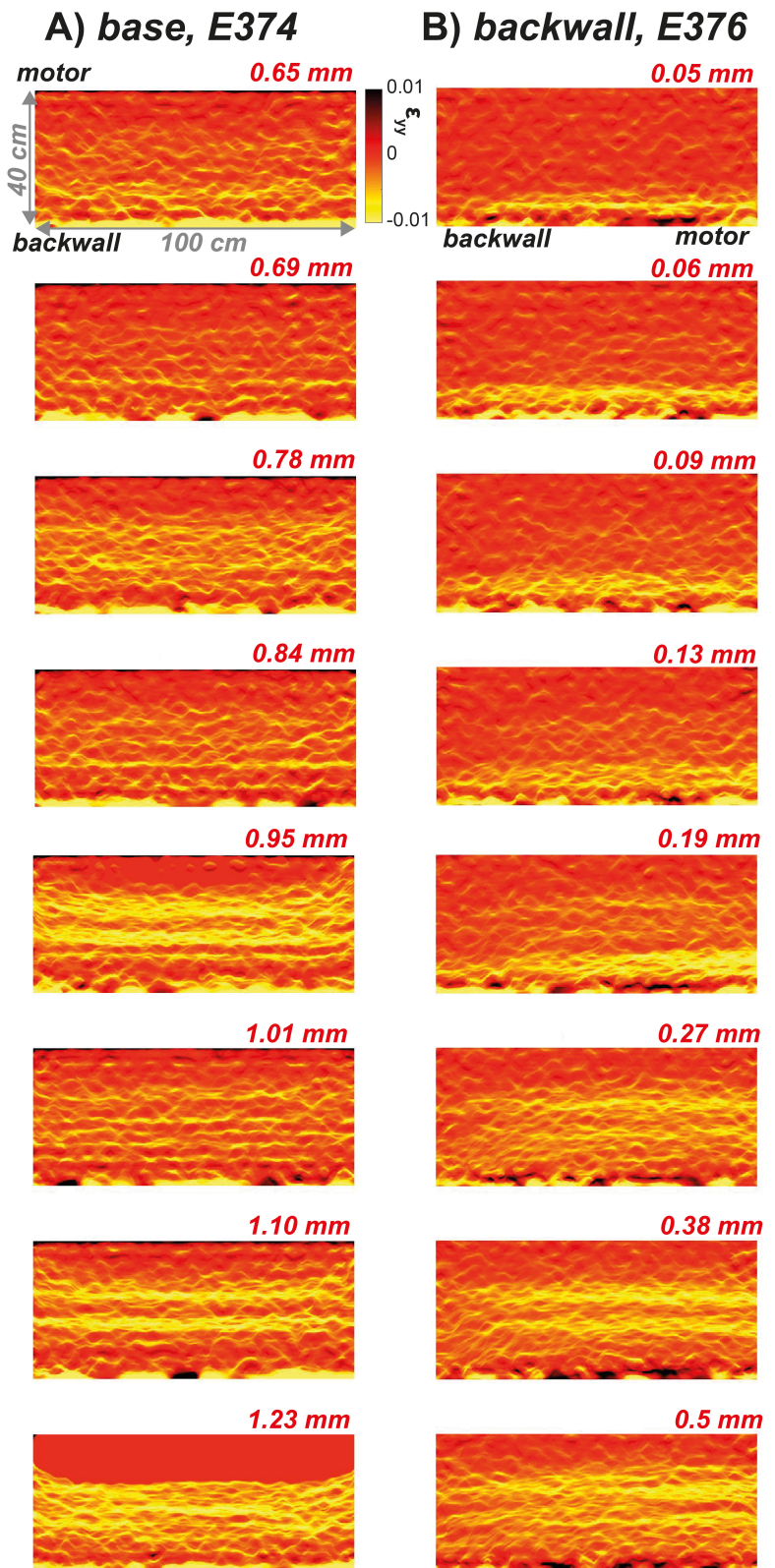
# The influence of detachment strength on the evolving deformational energy budget of physical accretionary prisms

Jessica McBeck[1, 2], Michele Cooke[1], Pauline Souloumiac[3], Bertrand Maillot[3], Baptiste Mary[3]

[1] Department of Geosciences, University of Massachusetts Amherst, MA, USA
[2] Now at: Physics of Geological Processes, The Njord Centre, Department of Geosciences, University of Oslo, Norway
[3] Département Géosciences et Environnement, Université de Cergy-Pontoise, Cergy-Pontoise, France

## *Overview*

This supplemental information contains one section of text, and six figures. Text S1 describes our calculation of the effective stiffness of the wedges. Figure S1 shows the calibration of the machine units of the strain gauges to normal force measurements. Figure S2 shows the results of the calculation of effective stiffness of the experimental wedges. Figure S3 shows the kinematic compatibility assessment used to determine the robustness of the DIC fields. Figure S4 shows the cumulative slip distribution along faults. Figure S5 shows the range of incremental work budget estimates using different assumptions. Figure S6 shows displacements fields from the top views of experiments with opposing configurations.

## *Supplemental Text S1:* **Effective stiffness**

In order to calculate the internal work done within the wedge, we must estimate the stress state within the wedge. We used Hooke's laws to estimate 2D stress tensors from strain tensors. These laws assume linear elasticity. Although the rheology of the sandpack within the fault zones is closer to plastic than linear elastic, it is reasonable to assume that the sand aggregate between the faults has a linear relationship between stress and strain. Preceding fault development, the stress-strain curves are approximately linear, indicating the linearity of this relationship.

To estimate the effective stiffness of the sand wedges, we calculated the normal stress exerted on the load-bearing area of the backwall and the horizontal longitudinal strain within the sandpacks preceding thrust faulting. We used the normal force measured on the backwall (Fig. 3) and an effective height of the load-bearing area of 4 cm, equal to the height of the rectangular sandpack. Calculating the horizontal contraction requires the displacement of the edge of the box and the length of the contracting region. We measured the horizontal displacement of the backwall recorded in the DIC displacement fields. We considered the full length of the sandbox (90 cm) as the length of the compacting region. Selecting a load-bearing height of 4 cm and contraction region length of 90 cm reflects the goal of calculating the effective stiffness throughout the wedge, and not only near the backwall or sidewalls. Although high magnitudes of horizontal compression were localized into different volumes in the experiments with opposing apparatus configurations (Fig. 9), the force exerted on the backwall was a result of force networks that span the length of the sandpack from the backwall to the opposite wall. Below, we investigate the influence of using a smaller compacting length (20 cm) to estimate stiffness because we observe the highest contraction within a volume of this length prior to faulting. From

the horizontal displacement of the backwall observed in the DIC fields from both sides, we found the average of the strains from the left and right sides as representative of the strain.

These estimates of the effective stiffness (~1 MPa) (Fig. S2) exceed previous estimates (0.11-0.25 MPa) of the effective stiffness of wedges built with an UCP depositor (*Herbert*, 2014). **The difference may arise because from the different areas over which the contraction is estimated. The calculation of 1 MPa uses the entire length of the sandpack whereas *Herbert* (2014) use only the region of compaction near the moving wall.**

**Here we assess the impact of using a smaller compacting length to estimate the effective stiffness. Gradients in the displacement fields observed at the top of the sandpack indicate that the largest magnitudes of contraction are localized within a minimum of 20 cm from the backwall, and spread to further distances from the backwall (Fig. S6). Estimating the effective stiffness of the sandpack with 20 cm as the length of the compacting region reduces the stiffness estimates to 0.13-0.26 MPa in agreement with *Herbert* (2014). Assuming 0.25 MPa as the effective stiffness in the calculations of $W_{int}$ decreases the average incremental $W_{int}$ by 0.007 mJ from the average $W_{int}$ calculated using 1 MPa (0.009 mJ) produced in experiment E376. Consequently, assuming a smaller effective stiffness results in smaller estimates of incremental $W_{int}$, and so does not change the general conclusion that $W_{int}$ comprises the smallest portion of the energy budget.**

Laboratory uniaxial compression tests of dry sand aggregates estimate stiffness that exceed the estimates from these UCP experiments. Dry sand in uniaxial compression tests with 50 loading-unloading cycles has apparent stiffness ranging from 100-400 MPa in the first cycle (*Klinkmuller et al*., 2008, 2016). Geotechnical engineering studies provide additional constraints on the expected effective stiffness of aggregates of sand grains (e.g., *Roberston and Campanella,* 1983). Empirical relationships derived from normally consolidated sand produce estimates of effective stiffness at 50% failure stress from 10-50 MPa (*Baldi et al.*, 1981). However, the estimates of bulk stiffness from these tests will likely exceed the effective stiffness within experimental wedges, where the sandpack is unconfined and free to uplift. If the upward movement of the sand grains were restricted in the sandbox experiment, the applied backwall displacement would produce greater backwall force than in the present unconfined configuration, producing higher estimates of effective stiffness that would be closer to confined laboratory measurements.

## Supplemental Figures

**Figure S1**

Calibration used to measure physical backwall force. A) Uniaxial strain sensors were mounted on four plaques that are fixed to a rigid board, which lay adjacent to the backwall in the experiments. Each plaque (blue) contained four uniaxial strain sensors (white rectangles) that are fixed to the two metal arms mounted on the plaque. B) Calibration of strain gauges to known weights resulted in a linear relationship of machine strain units to weight ($R^2$=0.99).
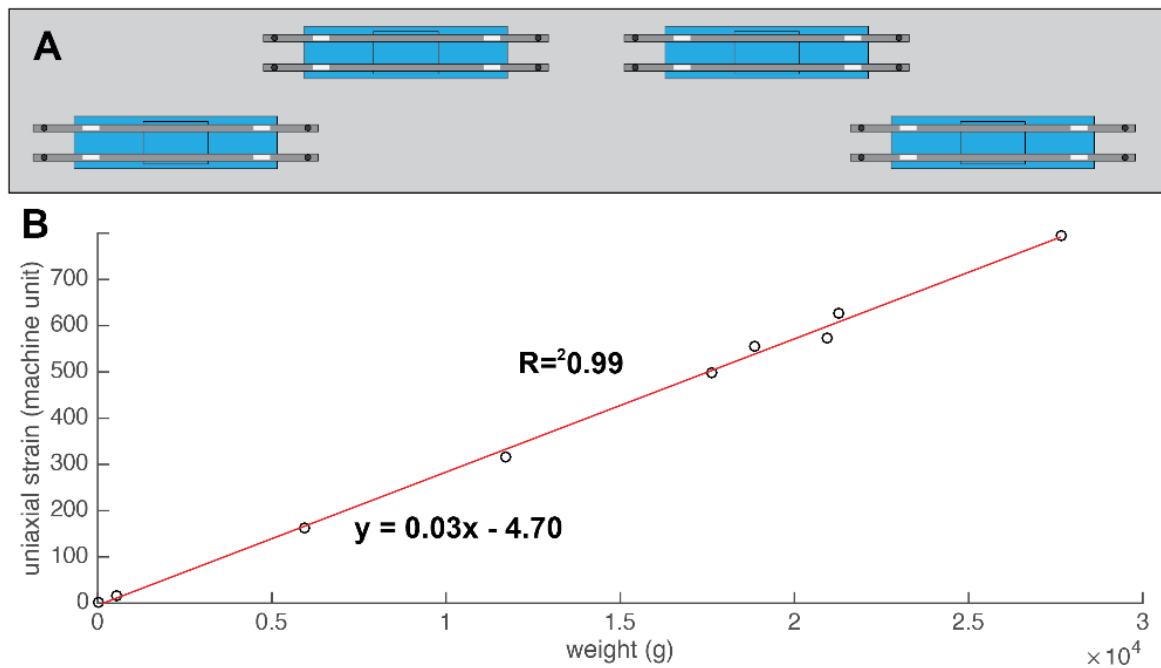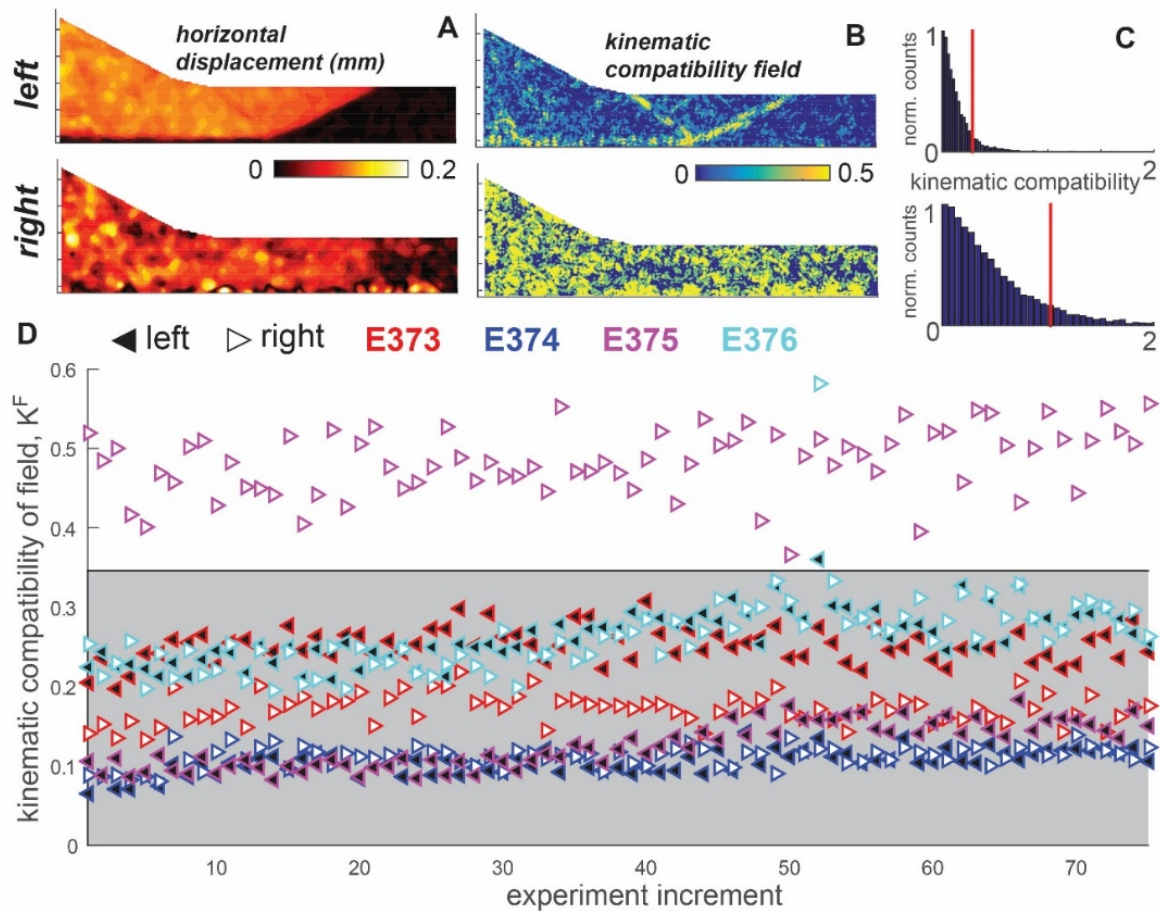
**Figure S2**

Estimates of effective stiffness of the physical accretionary wedges. A) Relationships between normal force exerted on backwall and backwall displacement measured from DIC fields from the top view camera. C) Resulting stress-strain relationships. Lines indicate tangent at 50% peak stress that determines the stiffness estimate. Linearity of the stress-strain curves suggest that using Hooke's laws provide a reasonable approximation of the stress state within the wedge outside of the fault zones.
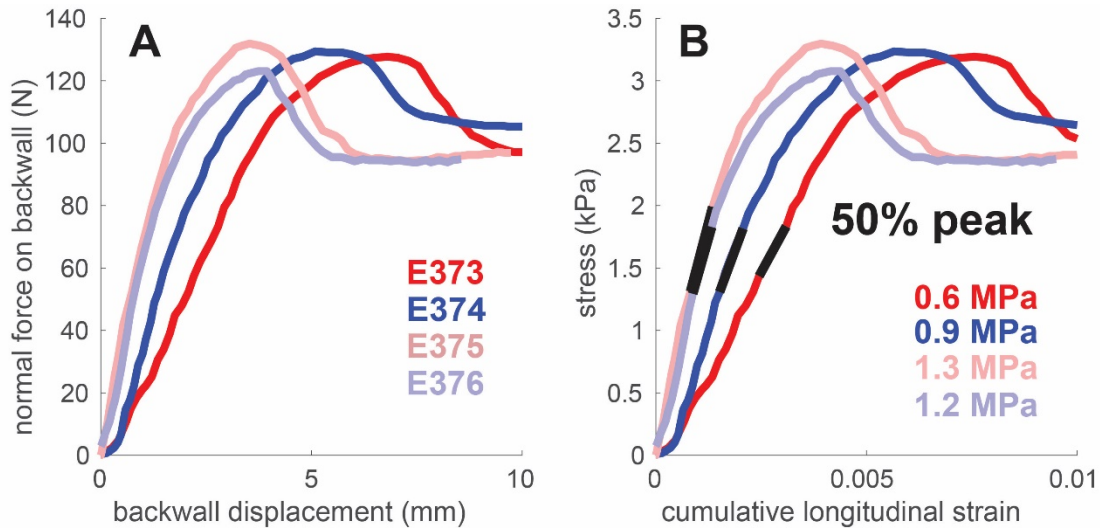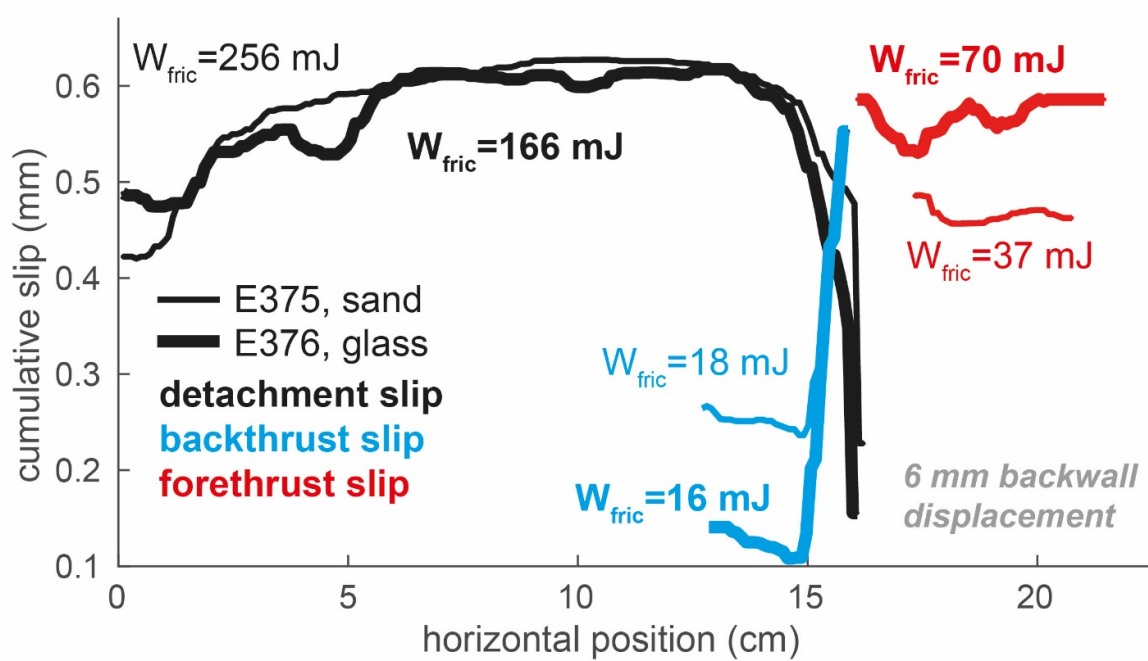
**Figure S3**

Kinematic compatibility of displacement fields indicates the amount of artificial noise in incremental displacement fields. Net displacement fields (A), and corresponding kinematic compatibility field (B) for example incremental displacement fields of left (upper row) and right (lower row) side of experiment E375. High $K$ was produced locally along faults in the left side displacement field, and in regions with higher artificial noise in right side displacement field. C) Histogram of kinematic compatibility, $K$, field for left and right sides reveal that the right side had higher magnitudes of $K$ than the left side. To compare the kinematic compatibility of each displacement field to other fields, we considered the mean plus one standard deviation of the $K$ field as the kinematic compatibility value representing that field, $K^F$, shown as red lines in (C). D) From each kinematic compatibility field, we identified $K^F$, and removed the fields from the analysis that had $K^F$ above one standard deviation from the mean of all $K^F$ from each incremental displacement field. Models within the gray region were thus considered reliable. Triangles pointing to the left (black triangle) and right (white triangle) show $K^F$ of displacement fields derived from the left and right sides of the experimental apparatus, respectively. Most of the displacement fields from the right side of experiment E375 were considered unreliable due to inadequate focusing of the associated camera. Consequently, we excluded the incremental displacement fields calculated for the right side of experiment E375 from further analysis.
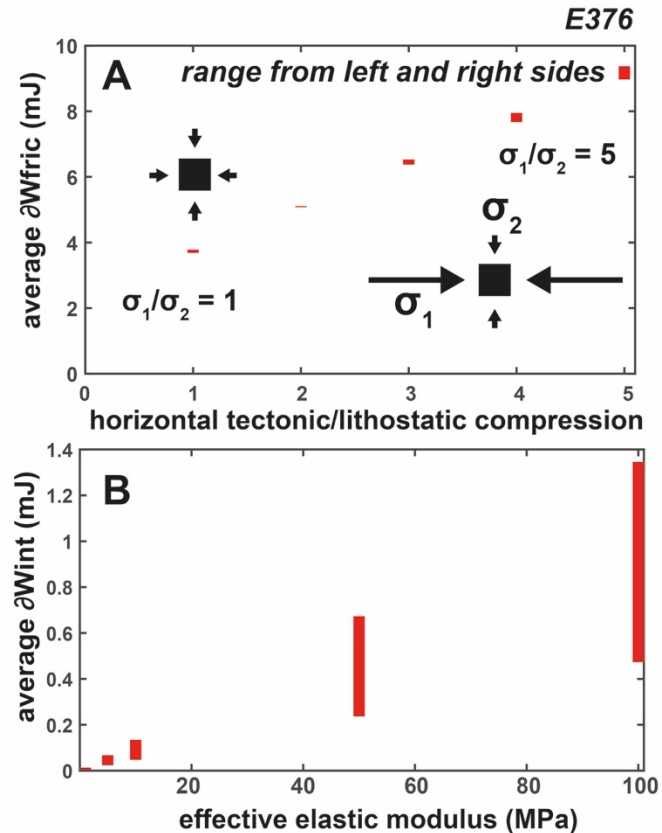
**Figure S4**

Cumulative slip distribution along detachment (black), backthrust (blue) and forethrust (red) in experiment with glass detachment (thicker lines) and sand detachment (thinner lines) at 6 mm of cumulative backwall displacement. Resulting contribution to $W_{fric}$ listed near corresponding fault. The higher slip and higher frictional coefficient of the detachment and lower slip on the backthrust in the glass detachment compared to the sand detachment experiment produced the lower frictional work in the glass detachment experiment relative to the sand detachment experiment.

**Figure S5**

Influence of stress state and effective stiffness assumptions on the calculation of $\delta W_{fric}$ (A) and $\delta W_{int}$ (B). Top and bottom of red bars show the average incremental work budget component calculated on the left and right sides of experiment E376. A) Average $\delta W_{fric}$ using different assumptions of the ratio of the horizontal normal compression, $\sigma_1$, and lithostatic stress, $\sigma_2$. We assumed that $\sigma_1/\sigma_2 = 1$, but $\sigma_1$ may be $> \sigma_2$. However, this ratio will likely remain <3 preceding Coulomb shear failure at the deepest portion of the sandpack, 4 cm of 1700 kg/m$^3$ density sandpack, $\sigma_2 = 0.6$ kPa. Thus, the potential difference in the reported and true $\delta W_{fric}$ may be 20%, with 4 mJ when $\sigma_1/\sigma_2 = 1$, and 6 mJ when $\sigma_1/\sigma_2 = 3$. B) Average $\delta W_{int}$ using different assumptions of effective elastic modulus used to estimate stresses from strains. Increasing the effective stiffness from the measured 1 MPa to 100 MPa does not increase $\delta W_{int}$ sufficiently to make it exceed the contributions of the other components of the energy budget. Decreasing the effective stiffness from 1 MPa to 0.25 MPa (estimated using a smaller compacting length) reduces the average $\delta W_{int}$ from 0.009 mJ to 0.002 mJ.

**Figure S6**

Net displacements from top views of experiment A) E374 (moving base), and B) E376 (moving backwall). Time (and backwall displacement) increase from top to bottom. The backwall is located at the bottom of each image. The motor is located at the top in the moving base (A) and at the bottom in the moving backwall (B) experiment. Following thrust fault development, the thrust fault strike is sub-perpendicular to the backwall in both experiments with differing apparatus configurations. Consequently, the impact of sidewall friction drag on thrust fault geometry is minimal after the thrusts have localized across the full width of the sandpack.